

Variation of sediment supply by periglacial debris flows at Zelunglung in the eastern syntaxis of Himalayas since the 1950 Assam Earthquake

Kaiheng Hu^{1, 2}, Hao Li^{1, 2, 3}, Shuang Liu^{1, 2}, Li Wei^{1, 2}, Xiaopeng Zhang^{1, 2, 3}, Limin Zhang^{3, 4}, Bo Zhang^{1, 2}, Manish Raj Gouli^{1, 2, 3}

¹Key Laboratory of Mountain Hazards and Earth Surface Processes, Chinese Academy of Sciences, Chengdu, 610041, China

²Institute of Mountain Hazards and Environment, Chinese Academy of Sciences, Chengdu, 610213 610041, China

³University of Chinese Academy of Sciences, Beijing 100049, China

⁴Department of Civil and Environmental Engineering, The Hong Kong University of Science and Technology, Clear Water Bay, Hong Kong, China

Correspondence: Kaiheng Hu (khhu@imde.ac.cn)

ABSTRACT. Periglacial debris flows in alpine mountains are influenced boosted by strong earthquakes or climatic warming in alpine mountains and play a crucial role in delivering sediment from hillslopes and downslope channels into rivers. Rapid and massive sediment supply to rivers by the debris flows has profoundly influenced the evolution of the alpine landscape. Nonetheless, there is a dearth of knowledge concerning the roles tectonic and climatic factors played in the intensified sediment erosion and transport. In order to increase our awareness of the mass wasting processes and glacier changes, five debris flows that occurred at the Zelunglung catchment of the eastern Himalayan syntaxis since the 1950 Assam earthquake are investigated in detail by field surveys and long-term remote sensing interpretation. Long-term seismic and meteorological data indicate that the four events of 1950-1984 were the legacies of the earthquake, and recent warming events drove the 2020 event. The transported sediment volume indexed with a non-vegetated area on the alluvial fan reduced by 91% to a stable low level nearly 40 years after 1950. It is reasonable to hypothesize that tectonic and climatic factors alternately drive the sediment supplies caused by the debris flows. High concentrations of coarse grains, intense erosion, and extreme impact force of the 2020 debris flow raised concerns about the impacts of such excess sediment inputs on the downstream river evolution and infrastructure safety. In regard to the hydrometeorological conditions of the main river, the time to evacuate the transported coarse sediments is approximately two orders of magnitude longer than the recurrence period of periglacial debris flows.

1 Introduction

Glacier-related hazards are widely developed in alpine regions around the world, such as the Alps, Himalayas, Caucasus, Tianshan, and Andes (Huggel et al., 2004; Iribarren Anaconda et al., 2015; Petrakov et al., 2007; Richardson and Reynolds, 2000; Shen et al., 2013). These hazards, including ice/rock avalanches, periglacial debris flows, glacial lake outburst floods (GLOFs), and dammed lakes, have caused substantial economic and human losses in the high mountains and their surrounding area (Bajracharya and Mool, 2009; Hu et al., 2019; Tian et al., 2017; Yu et al., 2021). Under Especially in the context of climate

设置了格式: 字体: (中文)+中文正文 (宋体)

批注 [hL1]: Owing to the reorganization of the institute, the original first affiliation "Key Laboratory of Mountain Hazards and Earth Surface Processes, Chinese Academy of Sciences, Chengdu, 610041, China" has been removed. In addition, as the institute has relocated, the postal code has been updated to "610213."

批注 [hL2]: Reviewer 1
a) Line 11: The phrasing that the earthquake "triggered debris flows" should be improved. Earthquakes do not directly trigger debris flows but may prepare material for them. Ultimately, a significant amount of water is still needed for debris flows to occur.

Author's response:
Thank you for your suggestion. We have revised the phrasing accordingly and have also reviewed the rest of the manuscript to avoid similar expressions elsewhere.

change~~4~~, characterized by rising temperatures and more frequent increased-extreme precipitation events)(Castino et al., 2016; Frich et al., 2007; Giorgi et al., 2016; Luan and Zhai, 2023; Myhre et al., 2019), the high-altitude regions such as European mountains, high mountain Asia, and the Andes are undergoing rapid deglaciation that increases the magnitude and frequency of are increasingly affected by more destructive and frequent ice/rock avalanches and, as well as low-angle glacier detachments accordingly (Wang et al., 2024; Zhang et al., 2023).

Earthquakes, climate warming, geothermal heating, rainfall, and meltwater all directly trigger glacier-related hazards (Haeberli and Whiteman, 2021; Huggel et al., 2004). The Himalayan mountains, which are tectonically active and sensitive to climate change, have experienced many glacier-related disasters triggered by large-magnitude earthquakes or climate warming in recent years. For example, on the 25 April 2015 Gorkha earthquake triggered a catastrophic ice-rock collapse in Nepal's Langtang Valley, causing over 350 casualties (Kargel et al., 2016). Between 2017 and 2018, multiple ice-rock avalanches in the Sedongpu catchment, Milin County, Tibet Autonomous Region (TAR), China, which triggered large-scale glacial debris flows that twice dammed the Yarlung Tsangpo River (Hu et al., 2019; Jia et al., 2019; Li et al., 2022). On 7 February 2021, about $27 \times 10^6 \text{ m}^3$ of rock and ice collapsed and quickly transformed into a debris flow in Chamoli, Uttarakhand region of India, which killed more than 200 people and severely damaged two hydropower projects (Shugar et al., 2021). The rising frequency and magnitude of such disasters have profound hydrogeomorphic and socio-economic impacts on the high-altitude and surrounding regions, including sediment yield and transportation, alpine landscape evolution, river management, food and water security, hydropower utilization, and infrastructure construction (Evans and Clague, 1994; Kääb et al., 2021), leading to the challenges of transboundary hazards and international collaboration.

Periglacial debris flows, influenced triggered by earthquakes or climatic events, are a major agent of sediment evacuation from steeplands steep slopes to rivers in high-altitude mountains. These flows result in massive ice loss and sediment transport, causing long-term impacts on high mountain environment. The Institute of Mountain Hazards and Environment, Chinese Academy of Sciences (IMHE, CAS) reported that periglacial debris flows in the Guxiang catchment of southeastern Tibet transported a total of 200 Mm^3 of sediment into an upstream tributary of the Brahmaputra River between 1953 and 1999 (Wang et al., 2022). Similarly, the ice-rock avalanches of the Sedongpu in October 2018 delivered approximately 33.2 Mm^3 of sediment into the Yarlung Tsangpo River (Hu et al., 2019). The total mass loss caused by glacier-rock avalanches in Sedongpu between 2014 and 2018 reached $> 70 \text{ Mm}^3$ of glacier and rock and $> 150 \text{ Mm}^3$ of moraine deposits (Li et al., 2022). Furthermore, after the glacier detachment of the Sedongpu in 2018, a huge volume of $\sim 335 \text{ Mm}^3$ material was eroded from its glacier bed and transported into the Yarlung Tsangpo (Kääb and Girod, 2023). Such, sudden, massive sediment inputs greatly influence sediment transport capacity, knickpoint formation, river water quality, downstream floods, and delta progradation. For instance, the 2021 Chamoli event resulted in extremely suspended sediment as 80 times high as the permissible level in the Ganga River, $\sim 900 \text{ km}$ from the source (Shugar et al., 2021). Sediment fluxes have increased two- to eight-fold in many glacierized and peri-glacierized basins between the 1950s and 2010s (Zhang et al., 2022a). Until now, most of previous studies have focused on the residence time and transport of earthquake-triggered landslide sediment at an orogenic scale in no-glacierized

批注 [hL3]: Reviewer 1
b) Line 33: The statement “rising temperatures and increased extreme precipitation events” requires a citation.

Author's response:

Thank you for your suggestion. We cited the studies by Giorgi et al. (2016), Luan and Zhai (2023), Castino et al. (2016), and Frich et al. (2007) and Myhre et al. (2019) to demonstrate that in high mountain regions such as the Alps, the High Mountain Asia, and the Andes, and even globally, there is a regional trend of increasing extreme rainfall events under the context of climate warming. Correspondingly, we referenced several regional and global statistical studies (Wang et al., 2024; Zhang et al., 2023) to support the evidence that, under this context, the frequency and magnitude of glacier-related hazards have increased.

environments (Dadson et al., 2004; Dai et al., 2021; Parker et al., 2011; Wang et al., 2015). Little attention has been given to the sediment evacuation progress by post-seismic debris flows at a catchment in glacierized environments owing to relatively low likelihood of debris flows and absence of long-term site-specific data. In order to investigate the long-term effects of earthquakes on sediment evacuation in a glaciated catchment, the Zelunglung (ZLL) catchment, a tributary of the Yarlung Tsangpo river in southeastern Tibet that has large areas of temperate glaciers and disturbed intensely by the Ms 8.5 earthquake in 1950, is chosen as our study case. The catchment has long-term remote sensing imagery for interpreting glacier changes and associated debris flows and relatively well-documented records of at least four historical periglacial debris flows in 1950, 1968, 1972, and 1984 since the 1950 Assam earthquake (Zhang and Shen, 2011; Zhang, 1992). The most recent debris-flow event occurred on 10 September 2020, triggered by a small-scale ice-rock avalanche. It is believed that historical earthquakes and ongoing climate warming drove such events (Bessette-Kirton and Coe, 2020; Deline et al., 2015; Stoffel et al., 2024; Zhang et al., 2022b). Field surveys were carried out before and after the 2020 event, including three aerial photography sessions on 9 September, 11 September 2020, and 21 December 2022, using a DJI Unmanned Aerial Vehicle (UAV). Dynamic process and sediment characteristics of the 2020 event were examined with the details of aerial photos and field measurements. The ZLL glacier and alluviation fan changes were interpreted with high-resolution optical remote sensing images from 1969 to 2022. The non-vegetated area of the alluvial fan was used as an index to reflect the variation of sediment supply caused by the periglacial debris flows. By integrating with historical data on neighboring earthquakes, temperature, and precipitation, we analyzed the trend of periglacial debris flows over different periods. This case study is helpful for a better understanding of the controlling factors and sediment transportation of periglacial debris flows in High Mountain Asia (HMA).

2 Study area

The ZLL catchment (94°56'13.4"E, 29°36'25.6"N) at Zhibai Village in the China's TAR is a tributary on the right bank of the lower Yarlung Tsangpo River, originating from the west side of Namche Barwa massif (7782 m) in the easternmost part of the Himalayas. The main stream flows westward into the Yarlung Tsangpo at an elevation of 2810 m, with a local relief of 4972 m (Figs. 1b and 1c). It has a drainage area of 41.21 km² with a 17.9 km² glacier area. The catchment extends over 41.21 km² with 17.06 km² (41.4%) covered by glaciers (RGI 7.0) (Fig. 1c). High lateral moraines on both sides of the main glacier divide the drainage network into the main channel, south branch, and north branch (Fig. 1c). The south branch, with a total length of 9.8 km and an average gradient of 27.5%, originates from the southern cliff at an elevation of ~5900 m. Hanging glaciers on the ridge and freeze-thawing in the cold region make the study area prone to ice and rock avalanches (Fig. 1d).

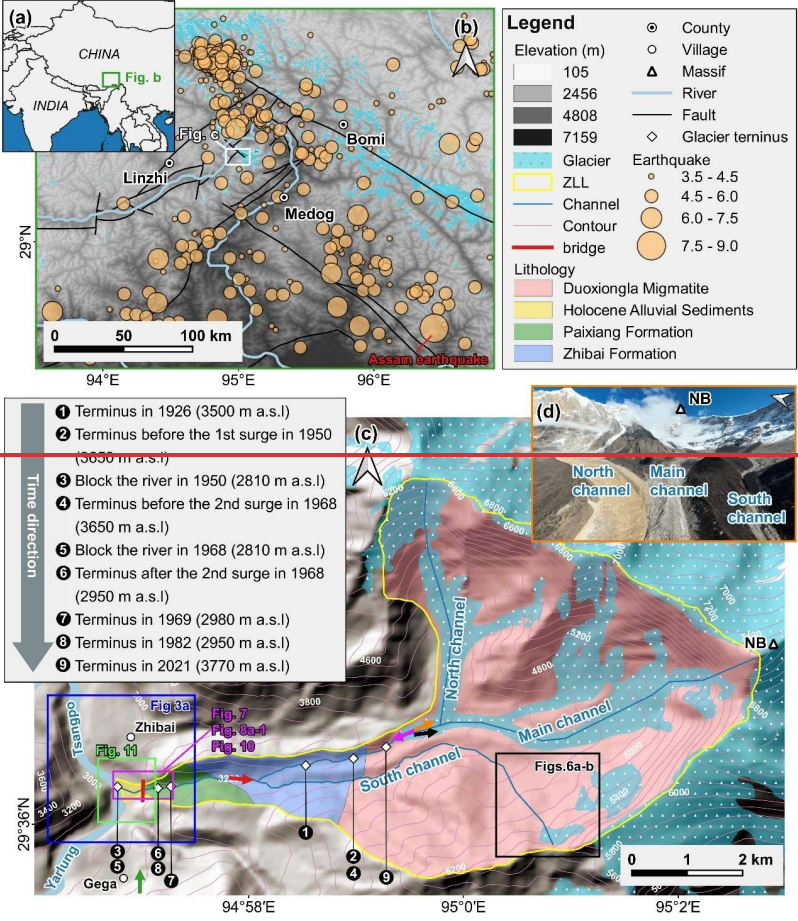
批注 [hL4]: Reviewer 1
c) Line 81: The percentage of glaciation within the catchment should be calculated and provided.

Author's response:
Thank you for your suggestion. We have added information on the proportion of glacier area. (based on the RGI7.0)

设置了格式: 字体: 加粗

批注 [hL5]: Reviewer 2
1. Page 3, Line 87. average gradient of 27.5% (not 275%)

Author's response:
Thank you for your careful review. Due to our oversight, we mistakenly wrote ‰ instead of %, and we have now corrected it.



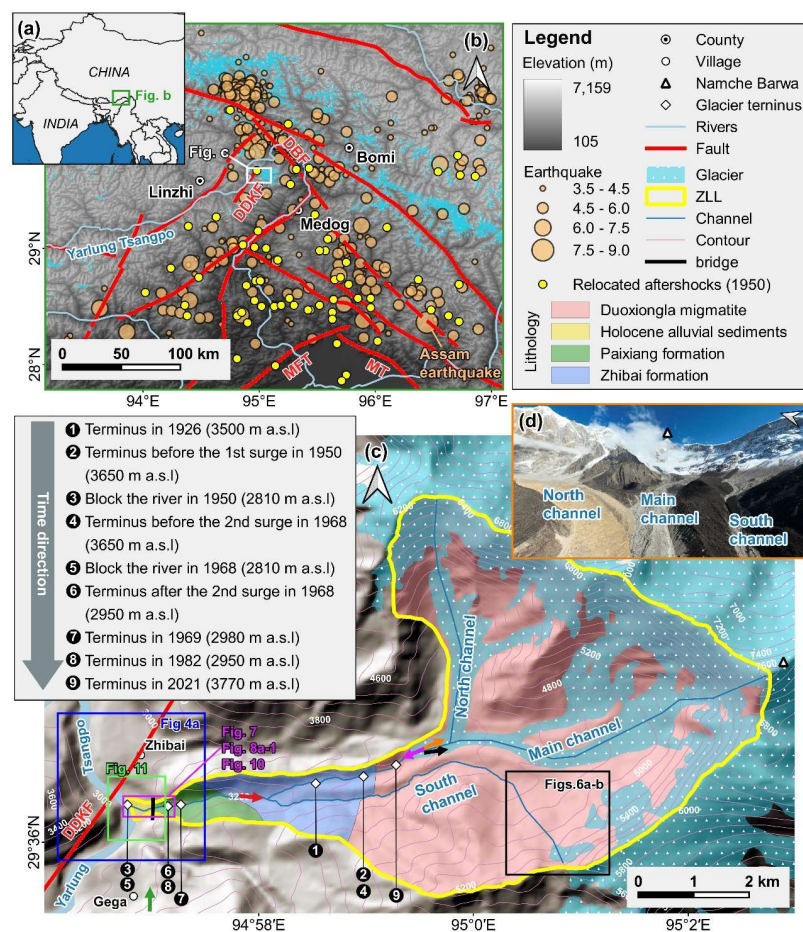


Figure 1: (a) Regional overview map of southeastern Tibet. (b) Regional settings of the eastern syntax of Himalayas, and historical earthquakes of southeastern Tibet. Fault data were obtained from Wu et al. (2024). Historical earthquakes from 1940 to 2020 were sourced from the United States Geological Survey (USGS) National Earthquake Information Center (NEIC) (<https://earthquake.usgs.gov/earthquakes/search/>). Relocations of aftershocks within the first four months following the 1950 Assam mainshock were taken from Coudurier-Curveur et al. (2020). MFT: Main Himalayan Frontal Thrust, MT: Mishmi Thrust, DBF: Damu-Bianba Fault, DDKF: Daduka Fault. (c) Topographic, geological and glacier terminus change maps of the Zelonglung catchment. The lithology refers to (Zhang and Shen, 2011) lithological information is based on Zhang and Shen (2011), and the glacier map is derived from the RGI 7.0 dataset (RGI, 2023). The orange, rose-red, green, black and red coloured arrows represent

批注 [hL6]: We have also updated the fault information in the figure and replaced the glacier distribution data from RGI 6.0 with RGI 7.0. In addition, the figure now includes updated references to other figures.

设置了格式: 字体: (中文) Times New Roman

设置了格式: 字体: (中文) Times New Roman

设置了格式: 字体: (中文) Times New Roman

设置了格式: 字体: (中文) Times New Roman

设置了格式: 字体: (默认) Times New Roman, (中文) Times New Roman

设置了格式: 字体: (中文) Times New Roman

设置了格式: 字体: (中文) Times New Roman

设置了格式: 字体: (中文) Times New Roman

设置了格式: 字体: (中文) Times New Roman

批注 [hL7]: Reviewer 1
d) Line 88: What time period do the referenced earthquakes cover? Although historical earthquakes are mentioned, the exact time frame would be interesting to know.

Author's response:

Thank you for your suggestion. The time span of the earthquakes shown in the figure 1b covers 1940–2020, which is consistent with the historical earthquake data used for statistical analysis later in the text. To avoid any potential confusion for readers, we have added this information to the figure caption.

设置了格式: 字体: (中文) Times New Roman

设置了格式: 字体: (中文) Times New Roman

设置了格式: 字体: (中文) Times New Roman

设置了格式: 字体: (中文) Times New Roman

设置了格式: 字体: (中文) Times New Roman

设置了格式: 字体: (中文) Times New Roman

设置了格式: 字体: (中文) Times New Roman

设置了格式: 字体: (中文) Times New Roman

设置了格式: 字体: (中文) Times New Roman

设置了格式: 字体: (中文) Times New Roman

设置了格式: 字体: (中文) Times New Roman

设置了格式: 字体: (中文) Times New Roman, 检查拼写和语法

设置了格式: 字体: (中文) Times New Roman, 检查拼写和语法

设置了格式: 字体: (中文) Times New Roman, 检查拼写和语法

设置了格式: 字体: (中文) Times New Roman, 检查拼写和语法

设置了格式: 字体: (中文) Times New Roman

设置了格式: 字体: (中文) Times New Roman

设置了格式: 字体: (中文) Times New Roman

设置了格式: 字体: (中文) Times New Roman

102 the view angle direction of figures 1d, 45a, 5b, 6c and 6d. (d) Aerial photo of the Zelunglung glacier and channels on December 21,
103 2022 (NB denotes the Namche Barwa massif).

104 The regional tectonic units are the Lhasa terrane, the Indus-Yarlung Tsangpo suture, and the eastern syntaxis of the
105 Himalayas from north to south (Hu et al., 2021). The catchment lies in the eastern syntaxis, which is uplifting at a rate of 5-10
106 mm/a (Ding et al., 2001). The exposed stratum in the ZLL is known as the Namche Barwa Group complex, which is composed
107 of Duoxiongla migmatite, Zhibai group, and Paixiang group gneiss. The Quaternary deposits consist of Holocene alluvium at
108 its outlet, thick layers of glacial till, and glacio-fluvial accumulation, especially hundreds of meters of huge thick moraine
109 layers with large boulders accumulated on both sides of the main channel (Fig. 1c) (Han and Feng, 2018; Zhang and Shen,
110 2011). Many active faults are distributed around the study area, such as the Main Himalayan Frontal Thrust (MFT) and Mishmi
111 Thrust (MT) Aniqiao-Medog Fault to the east, which is are considered the seismogenic faults of the 1950 Ms=8.5 Assam
112 earthquake (Coudurier-Curveur et al., 2020), Damu-Bianba Fault (DBF) NW-SE Xixingla fault that is the seismogenic fault of
113 the 2017 Ms=6.9 Milin earthquake (Hu et al., 2019), and Daduka Fault (DDKF) next to the ZLL downstream (Hu et al.,
114 2019) (Fig. 1b). Neotectonic movement makes this area highly susceptible to intense and frequent earthquakes.

115 This catchment lies in the rain shadow area of Mt. Namche Barwa, and its precipitation is controlled by the Indian Ocean's
116 humid monsoon through the Yarlung Tsangpo Gorge (Li et al., 2024b). The climate has a strong vertical difference: semi-
117 humid climate zone beneath 3200 m, cold temperate climate zone between 3200-4000 m, and cold climate zone above 4000
118 m. According to the data recorded at the Linzhi meteorological station 46.2 km west of the ZLL, the annual air temperature
119 with a mean value of 9.8 °C increases at an average rate of -0.36 °C/10a from 2000 to 2021, which is much higher than the
120 global average (Chen et al., 2015). The annual precipitation ranges from 514 mm to 972 mm, exhibiting notable inter-annual
121 variation, with no distinct trend over the past 20 years (Fig. 2).

设置了格式: 字体: (中文) Times New Roman

设置了格式: 字体: (中文) Times New Roman

设置了格式: 字体颜色: 红色

设置了格式: 字体: 加粗

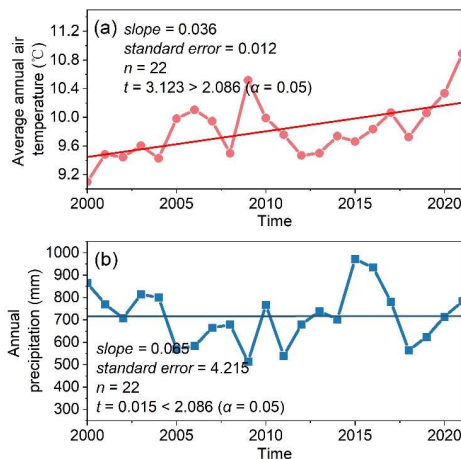


Figure 2: Annual temperature and precipitation data from 2000 to 2021 at Linzhi Meteorological Station. (Data source: <https://www.ncei.noaa.gov/maps/annual/>).

The ZLL catchment, characterized by unique geographical and climatic conditions, has hosted extensive glaciation and frequent glacial activity over geological time. The ZLL has experienced at least three glaciations in the Last Glacial Maximum (LGM), Neoglaciation, and Late Holocene (Hu et al., 2020). The LGM moraine extended into the Yarlung Tsangpo and dammed the river (Huang et al., 2014; Liu et al., 2006; Montgomery et al., 2004; Zhu et al., 2012). The glacier surges/debris flows - dammed lake - outburst flood disaster events since the last glacial period also had an important impact on the landform and paleogeographical environment of the Yarlung Tsangpo Valley (Wang et al., 2021a). The modern glaciers in this area are strongly influenced by the Indian monsoon and are highly sensitive to climate change. Hence, the ZLL glacier has advanced and retreated many times since the last century. The high instability and rapid changes of the glacier result in several glacier surges or calving events. As shown in Fig. 1c, the glacier snout was 3500 m a.s.l in 1926 (Ward, 1926). Since the 1950s, the ZLL glacier has experienced three surges or rapid advances (Zhang, 1985, 1992). The first surge occurred on August 15, 1950. Following the 1950 Assam earthquake, the terminus of ZLL Glacier advanced from 3650 m a.s.l to the Yarlung Tsangpo at 2810 m a.s.l with a horizontal displacement of up to 4.5 km. This event destroyed the Zhibai Village completely at the mouth of the Zhibai gully, killed 98 people, and formed an ice dam as high as tens of meters in the main river. The second surge occurred one afternoon in August or September of 1968 (corresponding to July 1968 in Tibetan calendar) when it was sunny (Zhang, 1985, 1992). The advance also resulted in a temporary ice dam in the Yarlung Tsangpo and deposited a glacial boulder of 4.0×5.0×5.5 m upstream of the dam-. (Zhang, 1985). It is worth noting that the position of the ice tongue before the second glacier surge has returned to the position before the first surge (3650 m a.s.l), and the peak velocity of these surges reached

批注 [hL8]: Reviewer 1

e) Line 107: While there is a clear increase in temperature, the precipitation data, in my opinion, shows no discernible trend. The cited precipitation trend of 0.65 mm/decade may be due to measurement uncertainty. Thus, its climatic significance is questionable. There are strong fluctuations and differences over time, which should be discussed more thoroughly. A general statement about increasing precipitation should be avoided.

Author's response:

We sincerely thank the Reviewer for their careful review. We agree with the Reviewer's point that the observed increase in precipitation rates may fall within the uncertainty range of the data. As suggested, we have re-analyzed the data by calculating the standard error of the slope (Fig. 2). The results show that the slope value is 0.065, the standard error is 4.215. The t-statistic value is approximately 0.0153, which is much smaller than the critical t-value of 2.086 at the significance level of α=0.05. This indicates that the trend is not statistically significant. In the revised manuscript, we have clarified that there is no significant trend in precipitation over the study period, aligning the discussion with the updated statistical analysis.

142 1.5 km/d. After the second surge, the main glacier split into 6 segments due to differential ablation, and the terminus of the
143 lowest segment of the glacier was at 2950 m a.s.l. The terminus of the lowest segment was about 2980 m a.s.l in 1969 as shown
144 by the Corona reconnaissance satellite images (Kääb et al., 2021). The terminus of the lowest part of the glacier had probably
145 been at 2950 m a.s.l before 13 April 1984 when an ice mass of 80000 m³ detached at 3700 m a.s.l and traveled horizontally
146 150 m, which was the third rapid advance of the ZLL glacier (Zhang, 1992). After that, no glacier surges or detachments were
147 recorded, but small-scale mountain torrents or debris flows occurred almost yearly (Zhang and Shen, 2011). At present, the
148 glacier terminus is about 3770 m a.s.l.

149 **3 Data and methodology**

150 **3.1 Data sources**

151 **3.1.1 Satellite images**

152 We collected a total of 30 different remote sensing images from various sources dating back to 1969, with resolutions ranging
153 from 1m to 15m (**Table 1**). The Keyhole images before 1982 were sourced from the Keyhole reconnaissance satellites
154 (<https://earthexplorer.usgs.gov/>), originally serving as the primary data source for the United States Department of Defence
155 and intelligence agencies for Earth imaging. These high-resolution images provide valuable visible data in the era without
156 commercial satellite imagery. Images from 1988 to 2007 originated from the Centre National d'Études Spatiales (CNES)
157 SPOT series data (<https://regards.cnes.fr/user/swh/modules/60>). Images from 2009 are sourced from the RapidEye series and
158 Planet satellites (<https://account.planet.com/>), which are known for their short revisit periods and high resolution. To
159 comprehensively document the historical debris flow activity in ZLL, we diligently chose images captured after every rainy
160 season (October to December) whenever feasible. Due to high cloud cover in the study area and limited availability of image
161 resources, we substituted images from the following year before May for specific periods with significant image data gaps
162 (e.g., before 2000) for those of the missing year (Li et al., 2017). Although the Landsat satellite series may offer more
163 continuous observational records, their relatively coarse resolution makes them unsuitable for our study area.

164 **Table 1: Data sources of the satellite images used in this study.**

No.	Date	Data sources	Resolution (m)
1	1969/12/08	Keyhole	1
2	1972/2/28	Keyhole	1
3	1973/3/26	Keyhole	1
4	1975/12/21	Keyhole	4
5	1979/4/10	Keyhole	1
6	1982/10/15	Keyhole	1

批注 [HL9]: Reviewer 1

f) Line 112: A subheading “satellite images” should be inserted here.

Author's response:

Thank you for your suggestion. We have inserted the subheading “3.1.1 Satellite images” and also listed the earthquake and meteorological data used under “3.1.2 Earthquake and climate.”

设置了格式: 字体: (中文) Times New Roman

带格式的: 标题 3

7	1988/2/20	Spot1	15
8	1989/12/1	Spot1	15
9	1990/12/21	Spot2	12
10	1991/11/25	Spot3	12
11	2000/11/17	Spot4	10
12	2002/12/5	Spot5	6
13	2004/12/28	Spot5	6
14	2005/10/10	Spot5	6
15	2006/12/21	Spot5	6
16	2007/11/29	Spot5	6
17	2009/12/22	RapidEye	5
18	2010/12/15	RapidEye	5
19	2011/11/23	RapidEye	5
20	2012/12/15	RapidEye	5
21	2013/12/7	RapidEye	5
22	2014/12/13	RapidEye	5
23	2015/12/6	RapidEye	5
24	2016/12/13	Planet	3
25	2017/12/11	Planet	5
26	2018/12/13	Planet	3
27	2019/12/7	Planet	3
28	2020/12/10	Planet	3
29	2021/12/12	Planet	3
30	2022/12/10	Planet	3

3.1.2 Earthquake and climate

Earthquake and climate datasets were used to investigate the potential linkages between these factors and debris-flow occurrence. Earthquake records within approximately 400 km of the ZLL catchment during 1940–2020 were obtained from the United States Geological Survey (USGS) National Earthquake Information Center (NEIC) (<https://earthquake.usgs.gov/earthquakes/search/>). In addition, gridded mean values of annual mean air temperature, summer air temperature, annual precipitation, and summer precipitation for the ZLL catchment during 1940–2021 were derived from the 1-km monthly precipitation and mean temperature dataset for China (1901–2021) (Peng, 2019, 2020). The reliability of these datasets has been verified against 496 independent meteorological observation stations across China (Peng et al., 2019).

设置了格式: 字体: (中文) Times New Roman

设置了格式: 字体: (中文) Times New Roman

设置了格式: 突出显示

设置了格式: 突出显示

批注 [hL10]: Reviewer 1
f) Line 112: A subheading “satellite images” should be inserted here.

Author's response:

Thank you for your suggestion. We have inserted the subheading “3.1.1 Satellite images” and also listed the earthquake and meteorological data used under “3.1.2 Earthquake and climate.”

173 3.2 Methodology

174 This study combines field surveys, aerial drone photography, and satellite imagery analysis to investigate debris flow events
175 in the ZLL catchment. Historical records of the four debris flows lack volume data. High-resolution orthoimages and digital
176 surface models are generated to assess terrain changes, while non-vegetated area (NVA) serves as a proxy for sediment volume
177 for time series analyses.—The integration of these methods provides detailed insight into the debris flow history and its
178 influencing factors.

179 3.2.1 Field surveys

180 We conducted three field surveys in at the ZLL between 2020 –and 2022. During the initial two survey, we conducted two
181 aerial drone photography works on September 9 and 11, 2020, using DJI MAVIC 2. Additionally, we measured downstream
182 channel cross-sectional morphology, debris flow particle characteristics, and the extent of damage to the Zhibai Bridge, and
183 sampled debris flow materials with size <100 mm on the accumulation fan in the second survey. A full 3D view of the ZLL
184 was captured with an unmanned aerial vehicle (UAV) in the third survey on December 21, 2022, a sunny winter dayThe first
185 survey (September 9, 2020) employed a DJI MAVIC-2 UAV to perform geomorphological photogrammetry of the downstream
186 channel and alluvial fan. During the second survey (September 11, 2020), we combined low-altitude UAV photogrammetry
187 with measurements from an IMETER LF1500A laser rangefinder to characterize the downstream channel morphology,
188 particularly near Zhibai Bridge, to analyze debris-flow erosion and deposition patterns. UAV photographs also provided close-
189 up views of inaccessible upstream sections. Tape measurements were used to determine bridge displacement and boulder sizes
190 on the fan, while low-altitude UAV orthophotos supported post-event interpretation of boulder distribution. Fine-grained
191 deposits (< 100 mm) were sampled from the fan apex for laboratory analyses. The third survey (December 21, 2022) used
192 UAV imaging to generate a complete 3D view of ZLL (Fig. 1d).

193 3.2.2 NVA interpretation

194 The inundation of debris flow on the alluvial fan often destroys vegetation cover and causes the affected area desertification
195 in a few years. Generally, the NVA depends on the flow magnitude. So, the NVA of the alluvial fan shortly after a glacial
196 debris flow can serve as a proxy of the volume of transported sediment. It should be noted that distinguishing fresh debris flow
197 deposits on an alluvial fan from pre-existing exposed surfaces in the surrounding area is challenging in satellite images due to
198 minimal color differences. Therefore, the NVA has some uncertainties in representing the real magnitude of the debris flows.
199 We employed a visual interpretation approach to delineate NVAs within the ZLL alluvial fan (Fig. 3). The Keyhole black and
200 white photos and the SPOT single-band black and white images show distinct tonal differences between vegetated and
201 unvegetated areas. In the true-color images obtained from RapidEye and Planet, the boundaries of NVAs are highly
202 conspicuous. Identifying the NVA is primarily based-Based on differences in color, tonehue, texture, and shading between
203 vegetated and non-vegetated unvegetated regions– areas in satellite imagery for a given year, we delineated the debris flow

- 设置了格式: 字体: (中文)+中文正文 (宋体)
- 设置了格式: 字体: (中文)+中文正文 (宋体)
- 设置了格式: 英语(加拿大)
- 设置了格式: 字体: (中文)+中文正文 (宋体)
- 设置了格式: 字体: (中文)+中文正文 (宋体)

批注 [hL11]: Reviewer 1
g) Lines 128–130: The procedure (cross-sectional morphology, debris flow particle characteristics, and the extent of damage to the Zhibai Bridge) should be described in more detail.

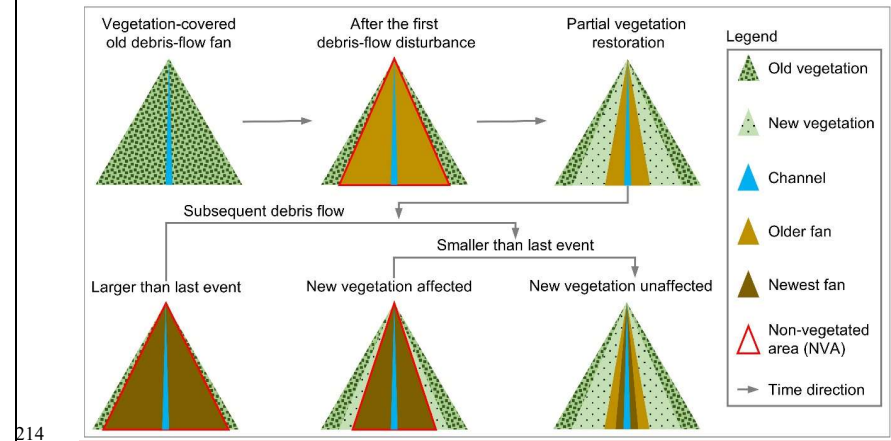
Author's response:
Thank you for your suggestion. We have provided a more detailed description in this section, including the specific locations of the survey, the sampling sites, and the instruments and methods used for the measurements.

批注 [hL12]: Reviewer 1
h) Lines 138–139: Potential sources of error and uncertainties should be discussed.

Thank you for your suggestion; we have added a discussion on errors and uncertainties in section “5.4 Limitation”

设置了格式: 字体: 加粗

204 inundation zone (i.e., NVA) for that year. When subsequent debris flows occurred and extended beyond the gully outlet, three
205 scenarios were observed: (1) the subsequent debris flow was of a larger magnitude, exceeding the previous inundation zone;
206 (2) the subsequent debris flow was smaller in magnitude but caused damage to newly established vegetation; and (3) the
207 subsequent debris flow was very small in scale, confined to the channel or a very limited area along its banks, and did not
208 affect vegetation. The third scenario is more appropriately classified as a minor seasonal flood with negligible sediment
209 transport compared with debris flows. Therefore, in our interpretation and statistical analyses, the NVA was restricted to the
210 first two scenarios (Fig. 3). The Keyhole black and white photos and the SPOT single-band black and white images show
211 distinct tonal differences between vegetated and unvegetated areas. In the true-color images obtained from RapidEye and
212 Planet, the boundaries of NVAs are highly conspicuous. The ZLL interpretation zone is limited to the region between the two
213 adjacent confluences of its upstream and downstream catchments with the main river.



214
215 **Figure 3. Conceptual illustration of non-vegetated area (NVA) interpretation**

216 Due to potential misalignment between remote sensing images from different sources, image matching is performed before
217 manual delineation of the NVAs (Cui et al., 2022). To eliminate the errors of geospatial locations of the images from different
218 sources, we used the 2020 Planet image as the reference image and selected ground control points with clear markers on this
219 image, such as road junctions, rivers, and typical topographic points. Third-order polynomial transformation is applied to
220 match the images from other sources accurately with the 2020 image, ensuring a positional error of less than 20 m relative to
221 the reference image. The original Keyhole images without geographical coordinates and projection system information are
222 georeferenced with the 2020 Planet image with the ground control points. We assume that the visual interpretation error of
223 NVAs is approximately one grid cell on either side of the boundary. Moreover, we verified the interpretation results of the
224 remote sensing images with the UAV orthoimages.

设置了格式: 字体: 加粗

批注 [hL13]: Reviewer 1
Line 140: This should be supported by a graphic. The methodology should be explained better using visual examples.

Author's response:
We have added a conceptual diagram illustrating the identification of NVAs in the manuscript, and provided a more detailed explanation

设置了格式: 字体: (中文) Times New Roman, 英语(英国)

设置了格式: 字体: (中文) Times New Roman, 英语(英国)

带格式的: 题注

225 **3.2.3 Drone image interpretation**

226 We employed Pix4DMapper and Arcmap10.8 to generate the UAV digital orthophoto maps (DOMs) and digital surface
227 models (DSMs), as well as to perform DSMs differencing. As ground control points (GCPs) were not deployed during drone
228 photography, we generated the DSM and DOM for September 9 in Pix4DMapper. Subsequently, 20 relatively stable points,
229 unaffected by debris flow events, were selected as GCPs in Arcmap using the September 9 DOM as a reference. These control
230 points were then applied in Pix4DMapper to generate the DSM and DOM for September 11. The DSMs of difference (DoD)
231 analysis was subsequently conducted in Arcmap. To determine the uncertainty in our DoD differencing result we follow
232 methods outlined in Shugar et al. (2021). Fifteen stable areas on old debris flow terraces adjacent to the valley floor, mainly
233 roads and unseeded farmlands, were identified. The standard deviation of DoD values within these areas was calculated and
234 used to estimate a two-sigma DoD uncertainty. The resulting uncertainty was estimated to be ± 0.493 m.
235 Utilizing post-event DOM captured on September 11, we visually interpreted the distribution of particles from the downstream
236 channel to the depositional fan on Arcmap10.8. High resolution and accurate color representation of the drone aerial images
237 enable us to reliably identify coarse particles (>50 cm). The interpretation results were compared with measurements obtained
238 with a caliper during the 2022 field survey.

239 **4 Debris-flow events and Sediment characteristics Results**

240 **4.1 Multi-periodic glacial debris flows**

241 Glacier surges or ice-rock avalanches can be transformed into debris flows that deliver massive amounts of sediment into the
242 river or deposit on the alluvial fan. Four large-magnitude debris flows accompanied by glacier instability occurred in 1950,
243 1968, 1973, and 1984 (Zhang, 1992; Peng et al., 2022). The 1968 event caused significant deposition in the alluvial fan,
244 characterized by a rough surface and indistinct channels (Fig. 34-a2). The magnitude of the 1950 event is perhaps more
245 significant than that of the 1968 event. According to Zhang (1992), the detached glacier in 1950 climbed over the ~ 80 meters
246 lateral moraine on the north at an elevation 4000 m and traveled downstream along the Zhibai gully (Figs. 34-a1 and Fig.
247 45a). Based on the erosional scar photo on the lateral moraine (Zhang, 1992) and the 2022 UAV photo, the residual depositional
248 area of the 1950 event in the upstream gully is $\sim 65,000$ m² (Fig. 45a). Although the glacier detachment happened in ZLL in
249 1950, most of the sediment deposited in the Zhibai channel and its alluvial fan. Fine sediment from the catchment can be
250 quickly transported downstream by river flows, but most coarse sediment is still left on the bank or the alluvial fans. There are
251 two terraces on the banks of the main river along the confluences of the ZLL catchment and Zhibai gully (Fig. 5a5b). T1 and
252 T2 terraces are ~ 10 m and ~ 150 m above the river level, respectively (Fig. 5b5c). The 1950 and 1968 events completely
253 dammed the Yarlung Tsangpo (Zhang, 1992). Compared with the 1969 Keyhole image (Fig. 3a4a), it is likely that the T1
254 terrace is the residual dam of the 1968 event. The debris flows in the 1950 glacier surge event eroded the T2 terrace (Fig. 34-
255 a2), which implies that the T2 terrace formed before 1950. The residual inundation area of the 1950 event is ~ 0.78 km² (Fig.

批注 [hL14]: Reviewer 1

c) For the differential elevation models shown, stable areas should also be presented, and the DoD values in those areas should be critically discussed. At minimum, the arithmetic mean, RMSE, maximum value, minimum value, and standard deviation should be reported.

Thank you for your suggestion. We have improved this part in the first revision. The reconstruction and differencing of DSMs are carried out in Pix4DMapper and Arcmap10.8. Since we did not deploy ground control points during drone photography, we generated DSM and DOM of September 9 in Pix4DMapper, and then selected 20 relatively stable points that were not affected by debris flow events as control points in Arcmap with DOM of September 9 as reference. These control points were then used in Pix4DMapper to generate the September 11 DSM and DOM. To determine the uncertainty for our UAV DSMs of difference (DoD) differencing result we follow methods outlined in Shugar et al. (2021). We identified a series of fifteen stable areas on old debris flow terraces adjacent to the valley floor (Mainly roads and unseeded farmlands) and retrieved the standard deviation of DoD values within these areas and used these to estimate a two-sigma DoD uncertainty. The resulting elevation uncertainty was ± 0.493 m, corresponding to a DoD volumetric uncertainty of $\pm 1.85 \times 10^4$ m³ (Line 422). Owing to the large extent of the study area, and to avoid redundancy while presenting geomorphic changes in the debris-flow impact zone more clearly, we did not include the results from the stable areas in the manuscript figure, but we provide them here in this response (Fig. S1).

... [1]

批注 [hL15]: Reviewer 1

3. Structure and Readability:
The text is very data-heavy, but at times difficult to follow. A clearer structuring of the results (e.g., subchapters for each individual event) would be helpful.

Author's response:
Thank you for your suggestion. We have revised the structure of the Conclusions section.

批注 [hL16]: Reviewer 1

6. Entire Results Chapter:
There is already extensive discussion included in the results chapter. A better separation between the results and the actual discussion would be desirable. This would give the paper a clearer structure and organization. Alternatively, the results and discussion could be merged into a single chapter. However, the current chapter structure suggests a clear separation between

... [2]

设置了格式: 英语(美国)

设置了格式: 字体: (默认) Times New Roman, (中文) Times New Roman

设置了格式: 英语(美国)

256 **5a5b**). If the magnitude is proportional to the inundation area, the flow magnitude of the 1950 event could be larger than that
257 of the 1968 event. From the 1972 and 1973 images, it is observed that fresh debris deposits inundated the north part of the fan
258 and did not go beyond the 1968 accumulation zone (**Figs. 34-a2, 34-b2 and 34-c2**). The same lobes and deposition boundary
259 and the marked collapse of the terminal glacier (**Figs. 34-b3 and 34-c3**) indicate that the so-called 1973 event mentioned by
260 Peng et al. (2022) likely happened in 1972. The fan in December 1975 exhibits significant brightness variations (**Fig. 34-d2**),
261 with pronounced channelization above the glacier (**Fig. 34-d1**), suggesting possible debris flow activity prior to this time.
262 Compared with 1975, the fan in 1979 displays a flatter terrain and more distinct channelization (**Fig. 34-e2**), indicating the
263 modification of the rough fan surface by debris flow activity. This also implies that, due to limited information at the time,
264 additional events during this period may have gone unrecorded. By 1982, noticeable vegetation had recovered in the middle
265 part of the fan (**Fig. 34-f2**). Concurrently, accelerated glacier ablation exposed lateral moraines (**Figs. 34-e3 and 34-f3**), while
266 the glacier terminus developed an extensive crevasse network (**Figs. 34-f4 and 34-f5**). These fractured ice bodies and moraine
267 materials, under the impact of ice avalanche at 3700 m described by Zhang (1992), contributed to the formation of the 1984
268 large-scale debris flow.

269

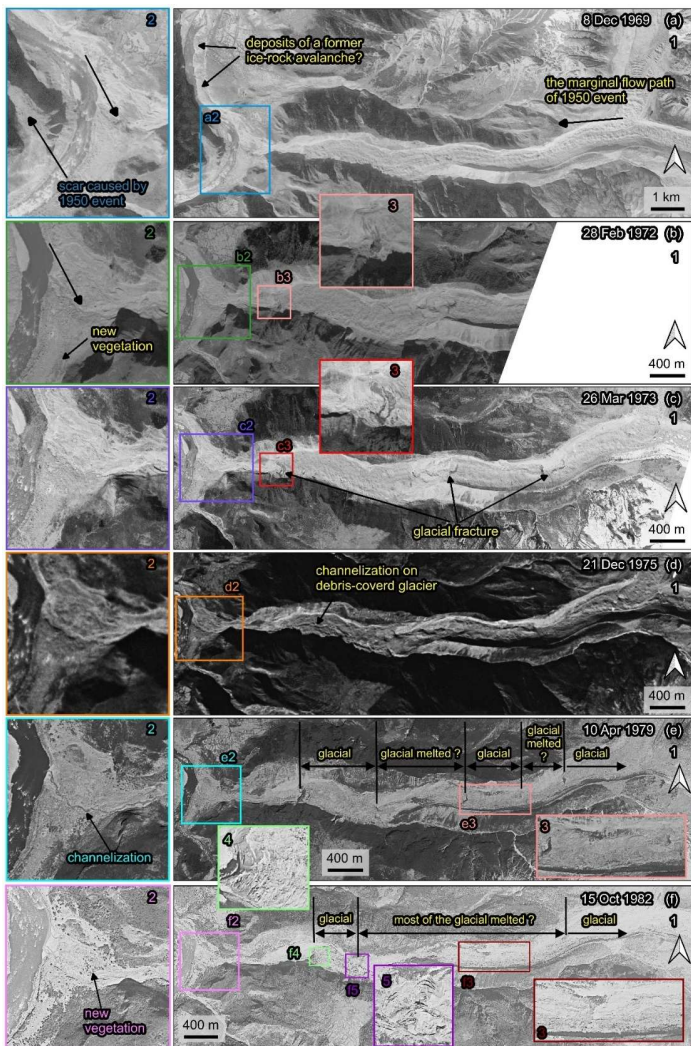


Figure 34: Variations of the Zelunglung alluvial fan and channel during 1969 – 1982. The images are taken from Keyhole reconnaissance satellites (<https://earthexplorer.usgs.gov/>).

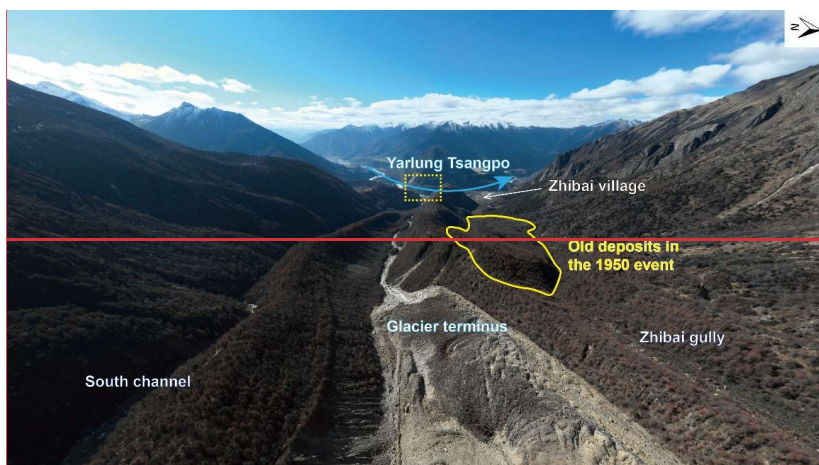


Figure 4: Aerial photo of the Zelunglung main channel on December 21, 2022, and the old deposits in Zhibai gully left by the 1950 event (the view angle direction is denoted by green arrow in figure 1c, and the dashed rectangle indicates the location of Figure 5b).



Figure 5: Two terraces on the banks of the main river. (a) Century Space's satellite image on 9 February 2021. (b) Picture of the terraces on the opposite bank of the Zelunglung taken on 8 September 2020. (T1 and T2 represent the terraces formed in

two different periods. The green arrow denotes the view angle direction of figure b)

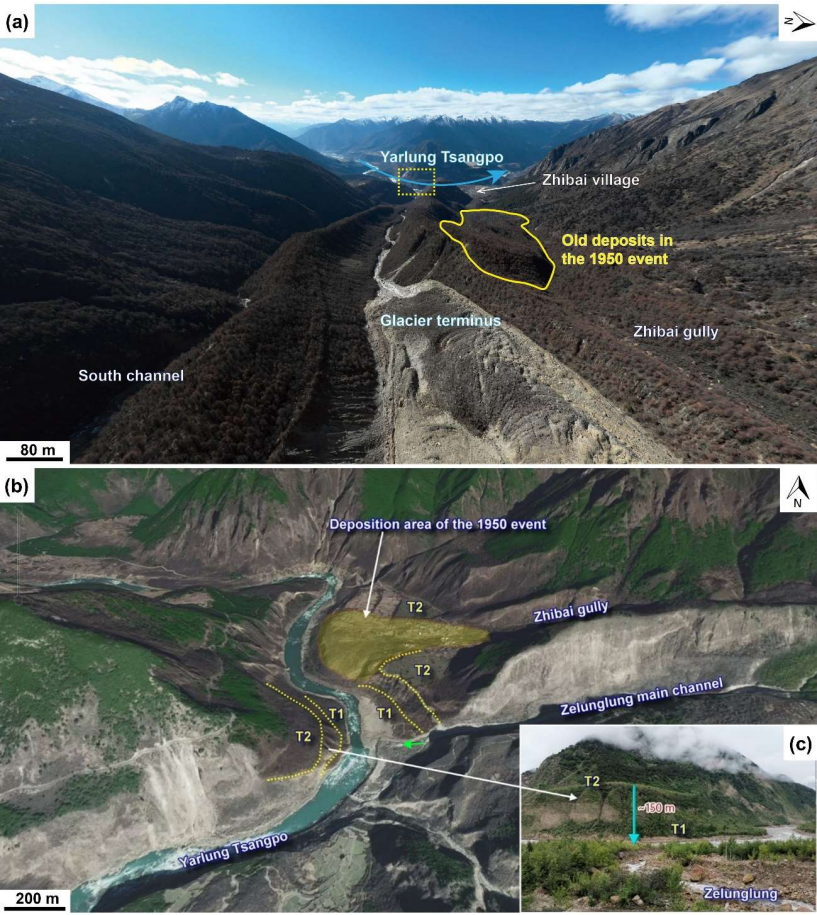


Figure 5: Remnant geomorphic evidence of historical glacial debris flows. (a) Aerial photo of the Zelunglung main channel on 21 December 2022, and the old deposits in Zhibai gully left by the 1950 event (the view angle direction is denoted by rose-red arrow in figure 1c, and the dashed rectangle indicates the location of figure c). (b) Century Space satellite image (9 February 2021) illustrating two terraces on the main river banks (the view angle direction is denoted by green arrow in figure 1c). (c) Picture of the terraces on the opposite bank of the Zelunglung taken on 8 September 2020. (T1 and T2 represent the terraces formed in two different periods. The view angle direction is denoted by green arrow in figure b).

设置了格式: 字体: (中文) Times New Roman
设置了格式: 字体: (中文) Times New Roman
设置了格式: 字体: (中文) Times New Roman, 非突出显示
设置了格式: 字体: (中文) Times New Roman
设置了格式: 字体: (中文) Times New Roman
批注 [hL17]: In order to reduce redundancy, these two figures have been merged into a single figure.
设置了格式: 字体: (默认) Times New Roman, (中文) Times New Roman
设置了格式: 字体: (默认) Times New Roman, (中文) Times New Roman
设置了格式: 字体: (中文) Times New Roman
设置了格式: 字体: (默认) Times New Roman, (中文) Times New Roman

287 An ice-rock avalanche triggered the recently documented glacial debris flow on Sep. 10, 2020. The 2020 ice-rock avalanche
 288 initiated on the top ridge of the south branch at an elevation of 5500 m. The scar area of initiated ice and rock was 1.35×10^4
 289 m^2 on the upper cliff (**Figs. 6a-b**). The initiated volume is estimated to be $7.0 \times 10^4 \text{ m}^3$ by using the bedrock landslide area-
 290 volume empirical relationship ($V = \alpha A^\gamma$; $\alpha = 0.186$, $\gamma = 1.35$) (Larsen et al., 2010). In the Google image on December 4,
 291 2017 (**Fig. 6-c2**), it can be seen that there is a protruding rock mass on the cliff below the unstable ice-rock block. The rock
 292 mass develops many lateral cracks, and the top is covered with fresh, weathered materials, indicating freezing severe
 293 weathering. The fallen ice-rock block partially disintegrated and impacted colluvial deposits on steep hillslope below the cliff
 294 at elevations 4570–4800 m, forming a muddy fresh area of 0.134 km^2 (**Fig. 6b**). This area is often covered by snow and ice,
 295 and the ice-snow melting water easily infiltrates into the debris-ice mixtures. Once the slope material was entrained into the
 296 mass flow, such a nearly saturated mixture could quickly turn into a debris flow. Peng et al. (2022) estimated a debris loss of
 297 1.14 Mm^3 in the scarp area except for the initiated ice and rock. But they mistake the hillslope below the cliff as the source
 298 area of the event. It is noted that there is an ice-rock residual of $\sim 7.14 \times 10^3 \text{ m}^3$ left under the cliff (**Fig. 6-b3**). That means the
 299 volume of the debris mass flowed downward into the south channel should include half of the initiated ice-rock mass and the
 300 debris loss of 1.14 Mm^3 . The entrained volume is at least 16 times the initiated volume.

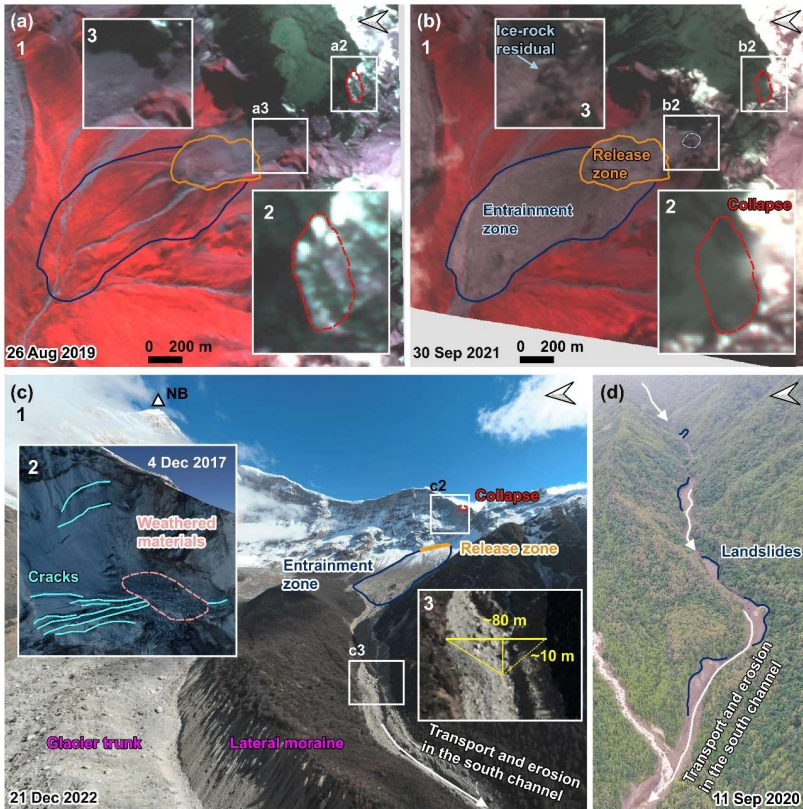


Figure 6: The initiation and propagation of the 2020 Zelunglung periglacial glacier debris flow. (a) The planet image of the initiation area before the event. (a2) enlarged region over the pre-collapse site. (a3) Enlarge the region over the hillslope before the collapse. (b) The planet image of the initiation area after the event. (b2) enlarged region over the post-collapse site. (b3) enlarged region over the hillslope after the collapse. (base data of a-b: © 2024 Planet Labs PBC) (c) An aerial photo of the source area and the south channel on 21 December 2022 was taken by the UAV. (c2) Google Earth imagery of the initiation area on 2 December 2017 (base data: ©Google Earth). (c3) The region was enlarged over the south channel on 21 December 2022. (d) An aerial photo of the downstream channel on 11 September 2020 was taken by the UAV.

When the debris flows traveled downstream, parts of old channel sediment and lateral moraines were eroded while some of the flow mass was deposited on the banks. The flows also triggered many small landslides on both banks of the middle stream (Fig. 6d). The blockage by large boulders and the induced landslides on the narrow channel may enlarge the magnitude of the debris flows in the end (Fig. 6d) (Cui et al., 2013; Liu et al., 2020). The UAV photo shows the influx of debris flows that

transformed from the entrained sediment and melting water exceeded the average water level of the south channel. The flow cross-section is ~ 80 m wide at the top and ~ 10 m high in the thalweg based on the UAV photo and OpenCycle topographic map (Fig. 6-c3). The peak discharge and frontal flow velocity reached 4700 m³/s and 11.4 m/s at the outlet (Peng et al., 2022). According to the description of local villagers, the first debris flow surge arrived at ZLL outlet at about 5:00 pm on September 10, and the second larger one arrived about one hour later. Two ice-rock avalanches with different volumes probably happened on the ridge and were the corresponding trigger of the downstream debris-flow surges. But it is more likely that there was only one ice-rock avalanche during the event, but a synchronization of the ice-rock impacts in the scarp area, and the channel blockage caused two debris-flow surges.

4.2 Sediment characteristics of the 2020 event

4.2.1 Difference between the initiation and the downstream areas

Periglacial debris flows can transport rocks or boulders not only in midstream steep channels but also in gentle downstream channels or alluvial fans. The sediment transportation capacity of the flows depends on flow hydrodynamics, grain composition, and topographic conditions. The 2020 ZLL event provides first-hand information for examining such sediment characteristics of the flows. Next, we present on-site data such as the size distribution of coarse grains, their impact, and erosion. The field evidence shows some features of periglacial debris-flow transportation that differ from fluvial transport.

There is a big difference between the sediment composition in the source and depositional areas. The initiated ice-rock debris and colluvial deposits on steep hillslopes consisted of angular rocks of various sizes. However, we observe that the deposits in the downstream areas are sub-rounded stones, and the downstream banks and channel bed are composed of sands and boulders up to several meters in diameter (Fig. 7). That means most of the angular rocks resided in the upslope or upstream channel and did not move downward. The angularity of the fragmented rocks reduced their mobility, and the attenuated overland flow had less transport capacity. The large sub-rounded or sub-angular boulders in the lower reaches came from the middle of the downstream reaches. We guess that grain segregation happened initially, and only fine parts of the ice-rock mass and melting water traveled downward the midstream. The resident angular rocks would be rounded gradually by the periglacial stream and transported downward by the subsequent floods or debris flows. The transportation mode of coarse grains is a kind of "Relay-race style", one event by one event.

Numerous boulders were on the channel and banks before the 2020 event, as seen from the aerial photo on 9 September 2020 (Fig. 7a). The in situ boulders were mobilized by the upstream flows and reorganized spatially. The boulders were prone to move together on the flat banks such as a flat storage yard near the bridge and the fan middle (Fig. 7b). The slope and flow depth are critical for the boulder's transport. Interstitial slurry among the boulders could separate from the boulders when the debris flows moved on a gentle slope or spread over an open fan (Fig. 7c). The interstitial slurry provided buoyancy for the boulders and reduced resistance between them and the bed. Once there was no interstitial slurry, the boulders quickly stopped quickly.

批注 [hL18]: Reviewer 2
2. Page 15, line 96. better: stopped quickly.

Author's response:

Thank you for your suggestion. We agree that "stopped quickly" is better. We have revised "quickly stopped" to "stopped quickly" accordingly.

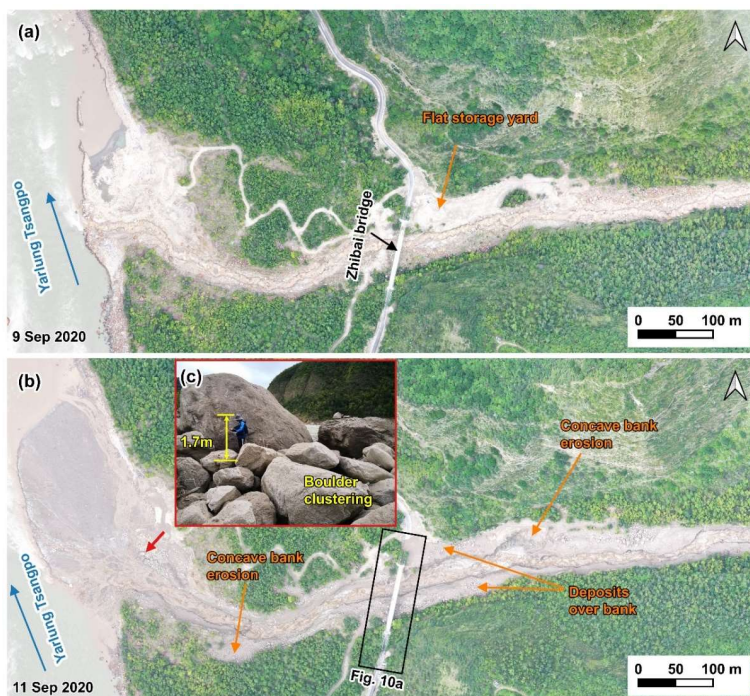


Figure 7: Comparison of pre-and post-event aerial photos on the downstream channel and alluvial fan. (a) the UAV photo on 9 September 2020; (b) the UAV photo on 11 September 2020; (c) On-site picture of the boulder clustering on 11 September 2020 (the camera angle direction is denoted by red arrow in figure b).

4.2.2 Grain-size distribution of coarse particles > 50 cm

In the downstream channel, with an average gradient of 13.8%, a relatively high velocity (11.4 m/s) enabled the flows to mobilize boulders of 5.0 meters in diameter (Costa, 1983). An 1125 m long straight reach from the first bend upstream of the bridge to the edge of the alluvial fan was chosen. Coarse particles > 50 cm on the deposition surface were visually interpreted from the orthophotos with a resolution of 0.17 m on September 11, 2020, after the debris-flow event. The long axis of the equivalent ellipse of these particles represents the particle size. Due to the limitation of resolution, only coarse particles with a long axis larger than 50 cm were counted (Fig. 8). A total of 3943 coarse particles were identified and divided into four size ranges of 50-100, 100-300, 300-600 and >600 cm. Spatial statistics of these particles were made every 25 m along the central flow line, and then 45 segments were divided.

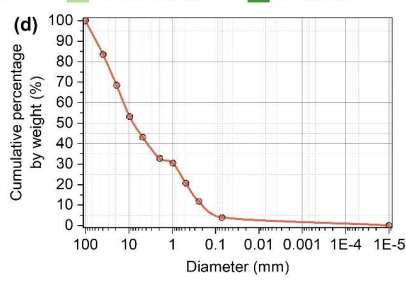
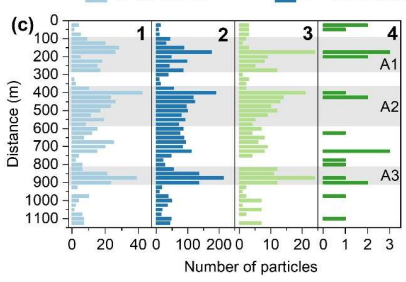
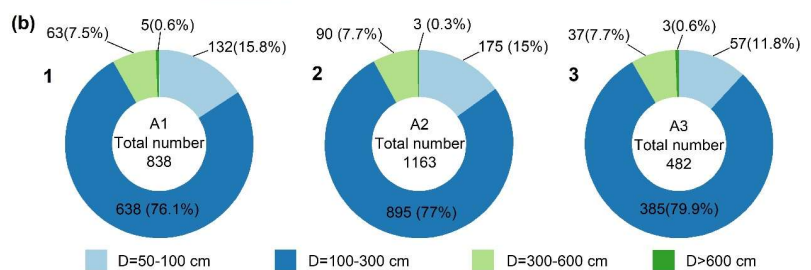
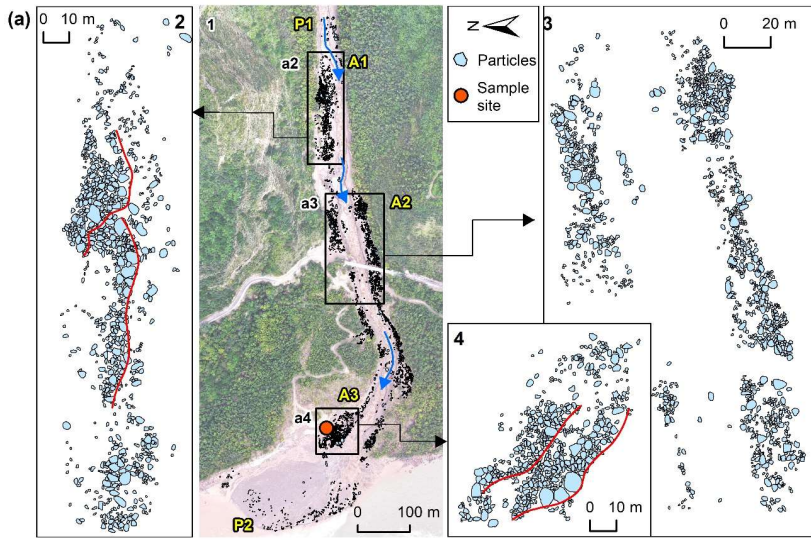


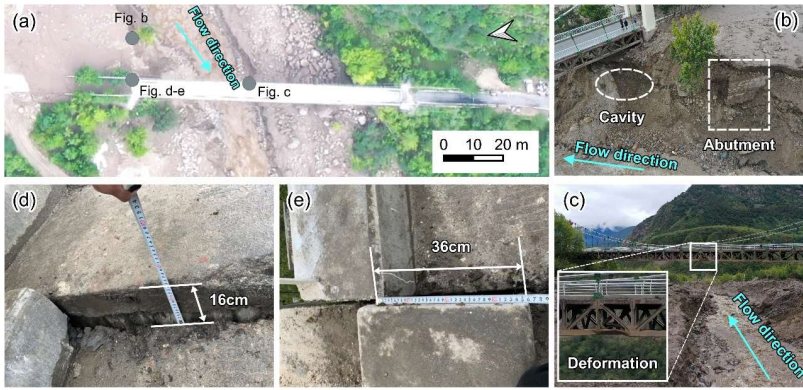
Figure 8: Distribution of the grain size. (a) The distribution of coarse particles along the channel and alluvial fan. P1 and P2 represent the places where the count starts and ends, respectively. A1-A3 are the three main deposition sites. The blue arrow is the direction of the debris flows. The bottom image is an orthographic image taken by a drone on September 10, 2020. The locations of the enlarged regions (a2)-(a4) are shown as black boxes. (a2)-(a4) enlarged region over the three main deposition sites A1-A3. Panels (b1)-(b3) show the counts of four groups of the particles in the three main deposition sites A1-A3. Panels (c1)-(c4) show the counts of four groups of the particles in the 45 segments along the channel from P1 to P2. Particles with diameters of 50-100 cm, 100-300 cm, 300-600 cm, and particles larger than 600 cm in panels b-c are shown in light blue, blue, light green, and green. (d) Cumulative grain size distribution of the on-site sample with size < 100 mm.

63% of the particles are concentrated in three zones A1, A2, A3 (Figs. 8a-b). The three zones are gentle banks or floodplains. The large stones easily slowed down when the flow depth and the velocity decreased on the edges of the debris flows. The composition of the particles in A1-A3 exhibits similar grain size distribution (Fig. 8b). The size of the most numerous particles is between 100 and 300 cm. The stones with the size > 600 cm are the least. The number of particles with 100-300 cm size accounts for 77.4% of the total. Likewise, the particles with sizes of 50-100 cm, 300-600 cm, and >600 cm, accounted for 14.3%, 7.7%, and 0.6% of the total, respectively. If the particle volume is estimated with the equivalent ellipsoid volume, i.e. $V = (4\pi abc) / 3$ (where a is major radius, b is short radius, c is polar radius and equal to b), the two groups of particles with the sizes of 100-300 cm and 300-600 cm have the largest volume. The spatial distribution of these particles in the 45 segments is shown in Figure 8c. The same four size ranges are used (50-100 cm, 100-300 cm, 300-600 cm, and > 600 cm). The particles with the first three sizes have three peaks in A1, A2, and A3 (Fig. 8c). The first peak is located on the right bank highland of A1. When the debris flows moved to A1, the flow depth was far higher than the channel depth. Many coarse particles were left on the highland. The second peak is located on both channel sides above Zhibai Bridge. When the debris flow enters the bend at a high speed, a large velocity difference will be generated on the concave-convex bank, i.e., the super-elevation effect (Chen et al., 2009). The debris flows produced the super-elevation effect when they moved to A2, a partially curved channel. Then, some coarse particles overflowed the channel and deposited on the A2 banks. The third peak is at the top of the alluvial fan. When the debris flows moved out the catchment outlet and had no boundary constraint, the other coarse particles gradually deposited from the fan top to the fan edge due to loss of kinetic energy. In the A1 highland, the particle size decreased toward the outer edge of the channel (Fig. 8-a2), while the coarse particles in A2 were poorly sorted (Fig. 8-a3). In A3, the coarse particles on the surface show the parallel superposition of two depositional units, and the particle size of each depositional unit generally decreases toward the outer edge of the channel (Fig. 8-a4). It reflects the gradual accumulation of multiple debris-flow surges (Sohn, 2000; Major, 1998). The two depositional units may correspond to the two successive debris flow surges in ZLL at 5:00 pm and 6:00 pm.

4.2.3 Impact and erosion

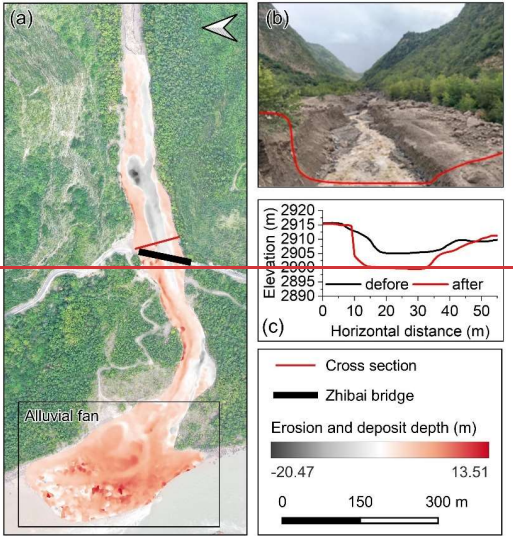
Debris flows usually have steep coarse-grained surge fronts (snouts) and inter-surge watery flows (McCoy et al., 2013; Yan et al., 2023). The periglacial debris flows in ZLL had similar spatial compositions. The granular flows (coarse-grained snouts) at the fronts exerted a powerful impact on obstacles, and the inter-surge watery flows or water-rich tails with relatively low sediment concentration played critical roles in erosion. The ZLL debris flows had a very high content of coarse particles and

394 wide distribution. The impact of the coarse particles witnessed by the damages of the Zhibai bridge, a 100m long cable bridge
 395 with a steel frame (**Fig. 9a**). The foundation of the bridge was exposed by the strong erosion capacity of the debris flows (**Fig.**
 396 **9b**). The middle steel frame was intensely impacted by run-up boulders and highly deformed (**Fig. 9c**). The concrete bridge
 397 body displaced 16 cm in vertical direction and 36 cm in horizontal direction (**Figs. 9d and e**). The velocity of the largest
 398 boulder with a size of 9.9 m was 12.6 m/s, and the impact force of the largest boulder was estimated to be 3.64×10^6 kN. The
 399 velocity of the debris flow at the selected cross section near the Zhibai bridge was 9.65 m/s, the peak value of debris-flow
 400 runoff was $1743.4 \text{ m}^3/\text{s}$ (**Fig. 10**) (Li et al., 2024a).

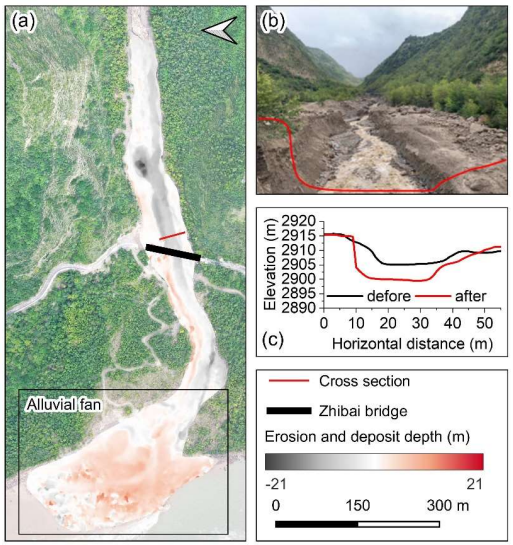


401
 402 **Figure 9: Damages to the Zhibai Bridge caused by debris flows (photos taken on 11 Sep 2020).** (a) The overview of Zhibai Bridge
 403 taken by UAV and the locations shown in photographs (b)-(e) taken with handheld cameras are shown in gray circles. (b) The photo
 404 of the damaged bridge foundation. (c) The photo of the damaged steel frame. (d) Photo of on-site measurements of the vertical
 405 displacement of the bridge. (e) Photo of on-site measurements of the horizontal displacement of the bridge.

406



407



408 **Figure 10: Geomorphic changes of the channel and alluvial fan after the debris flows of 2020. (a) Erosion and deposit depth caused**
409 **by the debris flows. The base map is taken by UAV on 10 Sep 2020. (b) Photo of the channel after the debris flows. The red line**
410 **represents the cross-section next to the Zhibai Bridge (photo taken on 11 Sep 2020). (c) Cross-sections before (black) and after (red)**
411 **the debris flows.**

412 A vibrating sieve measured one sample taken from the debris-flow deposits with the size < 100 mm. The concentration of
413 sediment finer than 0.075 mm is low, only 3.8% of the whole sample's mass (Fig. 8d). D50 and D90 of the sample are 8.3 mm
414 and 62.9 mm, respectively, as linearly interpolated from the sieve-measured data. The field evidence shows that the debris
415 flows strongly eroded the downstream channel. Comparing the DSMs before and after the 2020 event, the maximum erosive
416 depth was up to 20.47 m, and the mean erosive depth was 4.17 m (Fig. 10a). Peng et al. (2022) numerically simulated the final
417 erosion and deposition along the flow path. The maximum erosion depth was 7.41 m at the beginning of the downstream
418 channel. We think the simulation underestimates the erosion depth because the final erosion accumulates several erosive
419 watery flows. Lateral erosion **took place happened** nearly along the whole downstream channel. The channel width increased
420 from 17 m to 33 m at 70 m upstream of the bridge. The lateral erosion exposed the bridge foundation, and a cavity formed
421 below the pier (Fig. 9b). Concave bank erosion widened the channel by 14 m downstream. Based on the DoD, we estimated
422 that at least $12.8 \times 10^4 \text{ m}^3$ ($\pm 1.85 \times 10^4 \text{ m}^3$) of debris was transported out of the catchment (Fig. 10a). However, compared
423 with the study of Peng et al. (2022), the true volume may be seriously underestimated because part of the sediment may be
424 submerged **or washed away** by the Yarlung Tsangpo River, which is a bias caused by the difference in data acquisition time
425 **and the errors associated with DoD processing DEM/DSM resolution.**

426 **5.4.3 Multi-periodic Sedimentation-sedimentation in the confluence**

427 **Multi-periodic periglacial debris flows are strongly related to variations in the NVA of the alluvial fan. In practice, the NVA**
428 **includes a fixed part of the area inundated by the river and then is larger than the debris-flow depositional or flooded area (Fig.**
429 **11). Technically, the NVA caused by the main river cannot be completely excluded from the total area. However, the river**
430 **bank line was fixed from the 1980s to the 2010s when no large periglacial debris flows happened (Figs. 11b and c) (Zhang**
431 **and Shen, 2011). So, it is reasonably assumed that the variation of the river water level has no significant influence on the**
432 **NVA's change, and it represents the volume trend of the sediment transported by the debris flows.**

433 From the Keyhole satellite image in 1969, the deposited debris from the 1968 event resided on the confluence and covered a
434 2.5 km downstream reach of the Yarlung Tsangpo River from the junction (Fig. 3a4a) (Kääb et al., 2021). During 1969 – 1979,
435 the area of the accumulated fan kept at about 0.28 km². The 1972 image shows vegetation gradually developed from the edge
436 of the accumulation fan (Fig. 34-b2). A new channel developed along the 1972 deposition boundary across the middle of the
437 fan (Fig. 3b4b-2). Since then, the area without vegetation cover has reduced to 0.048 km² in 2005 and kept a slight fluctuation
438 from 1985 to 2005. It indicates that only rainfall-induced small-scale flash floods or debris flows occurred during 1985-2005,
439 which is confirmed by Zhang and Shen (2011). The NVA increased slowly, with a slight variation from 2005-2019. In 2020,
440 the NVA abruptly increased to 0.112 km² due to the ice-rock avalanche that happened on September 10 (Fig. 11). The

批注 [hL19]: Reviewer 1

k) Line 331: The value range of the DoD figure should be symmetrically centered around zero (e.g., -21 m to +21 m) to visually balance erosion and deposition and facilitate interpretation. Stable areas should also be shown, and a DoD error assessment should be carried out.

Author's response:

Thank you for your suggestion. We have updated the DoD range to -21 m to +21 m (Fig. 10). In our first revision, we quantified the DoD uncertainty as $\pm 1.85 \times 10^4 \text{ m}^3$ (Line 422). Owing to the large extent of the study area, and to avoid redundancy while presenting geomorphic changes in the debris-flow impact zone more clearly, we did not include the results from the stable areas in the manuscript figure, but we provide them here in this response (Fig. S1). ... [3]

批注 [hL20]: Reviewer 2

3. Page 20, line 70. Lateral erosion took place ...

Author's response:

Thank you for your suggestion. We agree that "took place" is better. We have revised "happened" to "took place" accordingly.

批注 [hL21]: Reviewer 1

k) Line 331: The value range of the DoD figure should be symmetrically centered around zero (e.g., -21 m to +21 m) to visually balance erosion and deposition and facilitate interpretation. Stable areas should also be shown, and a DoD error assessment should be carried out. ... [4]

批注 [hL22]: Reviewer 2

4. Page 20, line 74. Could part of the material be submerged? more likely it was eroded and washed away by powerful Yarlung Tsangpo stream.

Author's response:

批注 [hL23]: Reviewer 2
5. Page 21, line 76. Multi-periodic sedimentation ...

Author's response:

Thank you for your careful review. We have changed the initial letters of non-sentence-initial words to lowercase.

设置了格式: 英语(英国)

设置了格式: 默认段落字体, 字体: 加粗, (中文) 简体中文(中国大陆)

设置了格式: 英语(英国)

带格式的: 标题 2

441 expansion of NVA in 2020 demonstrates it is the most enormous debris flow event in the ZLL since 1972. At the same time,
442 the river channel narrowed down by more than 60 meters compared to before. The multi-periodic sedimentation in the ZLL
443 and Zhibai fans leads to rapids in this reach, forming a knickpoint before the river enters the Yarlung Tsangpo Grand Canyon.

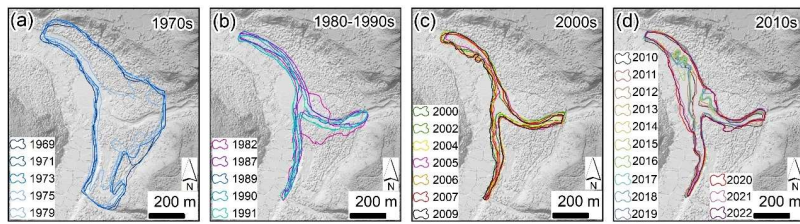


Figure 11: Evolution of the non-vegetated area in the Zelunglung alluvial fan from 1969 to 2022

6.5 Discussions

6.5.1 The dominant factor for debris flows and sediment yield

Strong ground vibrations caused by earthquakes can intensify cracking within the ice/rock mass, ultimately leading to the formation of substantial failure surfaces (Kilburn and Voight, 1998). Additional loading by earthquakes and coseismic-ice/rock avalanches could damage the englacial conduit and subglacial drainage system. These changes can cause dynamic alterations to the glacier's thermal sensitivity, exacerbating its instability (Zhang et al., 2022b). As critical solid material sources, these highly active ice/rock masses caused by seismic disturbance are prone to avalanches, calving, detachment and remobilization to form glacial debris flows (Deng et al., 2017; Zhang et al., 2022b). The data of seismic events since 1940 are collected from the United States Geological Survey (USGS) National Earthquake Center (NEIC) (<https://earthquake.usgs.gov/earthquakes/search/>) (Fig. 12a). It is observed that the four events in the ZLL in 1950, 1968, 1984, and 2020 were preceded by significant seismic activity (Fig. 12a). However, not all earthquakes influenced the instability of ZLL glaciers and hillslopes. Keefer (1984) presented an upper bound curve of maximum distance from epicenter to disrupted slide or fall (Fig. 13). In the absence of detailed fault information, we conducted a rapid and preliminary assessment of the impacts of historical earthquakes using this curve. Since 1940, only 12 earthquakes within a 420-km radius of ZLL fall below the bound curve, including the 1947 earthquake, the 1950 Assam earthquake and its aftershocks, the 1985 earthquake, and the 2017 Milin earthquake. Notably, the impact distance of a large earthquake can reach hundreds of kilometers. For example, the co-seismic landslides triggered by the 2015 Gorkha Mw 7.8 earthquake extended to a distance of over 130 km from the epicenter (Martha et al., 2017). The 1950 Assam earthquake, with its epicenter approximately 199 km from the ZLL, had a very high magnitude (Mw 8.6) and occurred in the tectonically active eastern Himalayan syntaxis. Coupled with subsequent high-magnitude aftershocks near the ZLL (Fig. 13), the seismic impact on the ZLL was significantly amplified despite the

批注 [hL24]: Reviewer 1

6. Entire Results Chapter:

There is already extensive discussion included in the results chapter. A better separation between the results and the actual discussion would be desirable. This would give the paper a clearer structure and organization. Alternatively, the results and discussion could be merged into a single chapter. However, the current chapter structure suggests a clear separation between results and discussion, whereas in the text, these two sections blur together, and the actual discussion is ultimately rather brief.

Author's response:

Thank you for your suggestion. We have reorganized the structure of the manuscript.

We moved the "4.1 Rapid glacier changes" section to the study area description, as it is based on literature review. The "5 Multi-periodic Sedimentation in the Confluence" section was incorporated into "4 Results." The final "4 Results" section is divided into three subsections: "4.1 Multi-periodic glacial debris flows," "4.2 Sediment characteristics of the 2020 event," and "4.3 Multi-periodic sedimentation in the confluence." We consider these three subsections to present direct conclusions derived from our methods, including the basic characteristics of historical debris flows, detailed sedimentary features of the 2020 event, and the interpreted distribution of non-vegetated areas (NVA).

In the Discussion, the original "6.1 The dominant factor and future risk" was split into "6.1 The dominant factor for debris flows and sediment yield" and "6.2 Debris flow recurrence intervals and future risk." We provide a more in-depth discussion of earthquake and climate influences, linking different events, NVA changes, and the effects of climate and seismic activity. In "6.2 Debris flow recurrence intervals and future risk" and "6.3 Effects on river geomorphology," we performed comparative analyses addressing reviewer comments on recurrence intervals, sediment mobilization, and downstream impacts on the river system. A new subsection, "6.4 Limitations," was added to discuss methodological uncertainties and directions for future research.

批注 [hL25]: Reviewer 1

2. Assessment of Climatic Control:

The attribution of the 2020 event solely to temperature rise is largely understandable but should be formulated more cautiously. The link between the sudden temperature increase (2.5 °C in 2018) and immediate ice/rock instability appears more speculative than causal.

Author's response:

Thank you for your suggestion. Yes, we agree with your perspective. In this revision, we have adopted a more conservative phrasing. In addition, we conducted a more in-depth analysis and found that the NVA has exhibited four peaks since 2000. These peaks likely correspond to the small flash-flood debris flow events described by Zhang et al. Interestingly, these peaks lag behind the summer temperature maxima by 2–4 years, which is consistent with the 2020 event occurring two years after the abrupt warming in 2018. Notably, similar lag phenomena have also been observed in other comparable regions (Deng et al., 2017; Stoffel et al., 2024). We consider this regular pattern as further evidence supporting the contribution of temperature.

466 distance. Although 13 earthquakes of $M_w > 5.1$ occurred in 1968 and 6 earthquakes of $M_w > 4.5$ occurred in 1984, none of
467 these seismic events fell within the range of influence as defined by the Keefer curve (Fig. 13). This suggests that these
468 earthquakes did not have a significant influence on the debris flow events of 1968 and 1984. Relocated aftershocks of the 1950
469 earthquake (Coudurier-Curveur et al., 2020) indicate that the seismogenic faults—the MFT and MT—extend their influence
470 well beyond the ZLL (Fig. 1b). This seismic event also contributed to triggered a prolonged period of debris flow activity,
471 persisting for decades, in Guxianggou, approximately 50 kilometers northeast of the ZLL (Du and Zhang, 1981). Although 13
472 earthquakes of $M_w > 5.1$ occurred in 1968 and 6 earthquakes of $M_w \geq 4.5$ occurred in 1984, none of these seismic events fell
473 within the range of influence as defined by the Keefer curve (Fig. 13). This suggests that these earthquakes did not have a
474 significant influence on the debris flow events of 1968 and 1984. The 1950 debris flow event was associated with directly
475 triggered by the 1950 Assam earthquake (Zhang, 1992), and the root causes of the 1968, 1972 and 1984 events were the
476 structural damage to the glacier and its exposure to lower altitudes with higher temperatures, both resulting from the 1950
477 earthquake. If including the inundated area of $\sim 0.78 \text{ km}^2$ in 1950, the alluvial area disturbed by debris flows or floods decreased
478 by 91% until 1990 (Fig. 12d). This means the earthquake effect becomes negligible 40 years later, as the under stability of the
479 glacier/materials caused by the earthquake may have improved. While the highest frequency of earthquakes occurred near the
480 time of the 2020 event, they could be ignored due to their small magnitude ($M_w \leq 5.2$) and long distance ($> 30 \text{ km}$) (Fig. 13).
481 This is because even the 2017 M_w 6.4 Milin earthquake, with an epicenter 24 km from the ZLL, had a very limited impact
482 area (310 km^2 , $\sim 10 \text{ km}$ impact radius) (Hu et al., 2019), and there were no report or sign of such glacier-related hazards in the
483 ZLL. However, there are direct proofs that the Milin earthquake caused the 2018 glacier surges and extra large-scale debris
484 flows in the Sedongpu (Hu et al., 2019; Zhang et al., 2022b), 25 km downstream of the ZLL.

批注 [hL26]: Reviewer 2

6. Page 22, line 11. In such case more important is not the distance from the epicenter, but distance from the earthquake source (causative fault). Energy is released not from the point (hypocenter), but from the entire source.

Author's response:

We agree with your comment. The maximum distance from the fault rupture zone to landslides indeed provides a more accurate upper bound, since seismic energy is released along the entire fault. We cited the long-distance effects of the 2015 Gorkha earthquake to illustrate the possible influence of the Assam earthquake on ZLL; however, we acknowledge that this comparison may not be appropriate, given the potential differences in causative fault length between earthquakes.

Nevertheless, previous studies have confirmed the strong impact of the 1950 earthquake on the ZLL region. The 1950 Assam earthquake occurred at the Assam sub-Himalayan syntaxis and was triggered by rupture of the Mishmi Thrust (MT). Coudurier-Curveur et al. (2020) recalibrated the aftershock distribution within the first four months following the mainshock and revealed proximal aftershocks near the ZLL basin (about 1 km away) with magnitudes up to M_w 5.5. The 1950 earthquake directly caused severe damage to houses and temples in this region. The northernmost aftershocks further suggest that the influence of the MT fault extended beyond its distance to ZLL.

In the absence of detailed fault information, the epicentral distance curve can still serve as a quick and approximate estimation tool. For this reason, we have retained Figure 13 in the revised manuscript.

设置了格式: 字体: 加粗

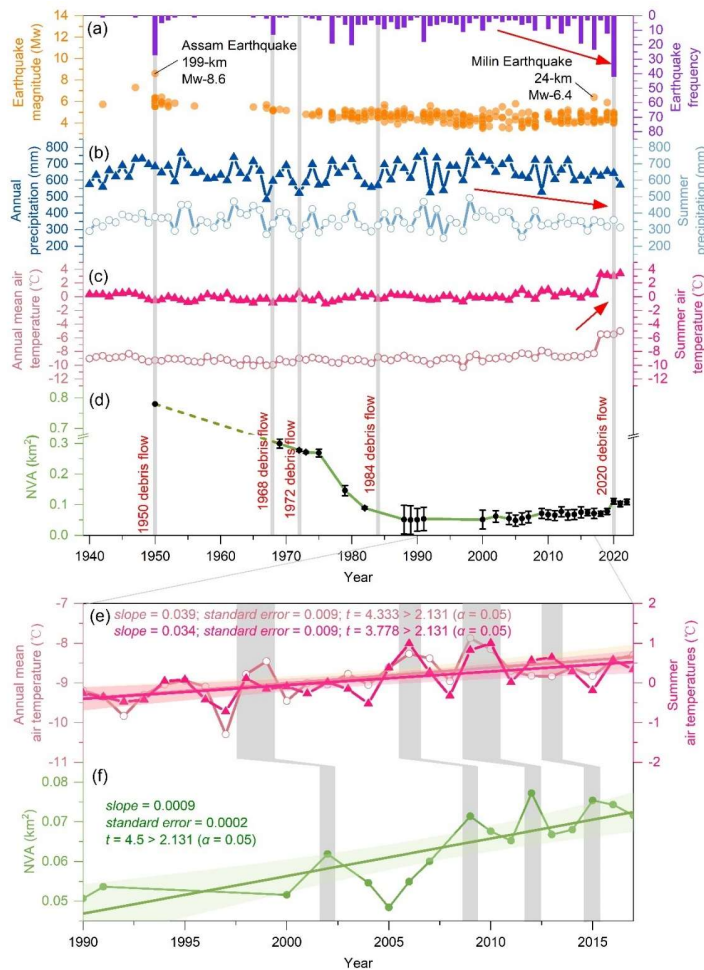


Figure 12: (a) Seismic events within a 200 km distance to the Zelunglung from 1940 to the present. (b) Changes in the annual mean and summer air temperatures in the Zelunglung from 1940 to the present. (c) Changes in the annual and summer precipitation in the Zelunglung from 1940 to the present. (d) Changes in the non-vegetated area of the Zelunglung alluvial fan from 1969 to the present (although the deposition of the 1950 event did not happen at the Zelunglung's outlet like the later events, we plot the NVA of the 1950 event as the starting point). (e) Changes in the annual and summer precipitation in the Zelunglung from 1990 to 2017. (f) Changes in the non-vegetated area of the Zelunglung alluvial fan from 1990 to 2017.

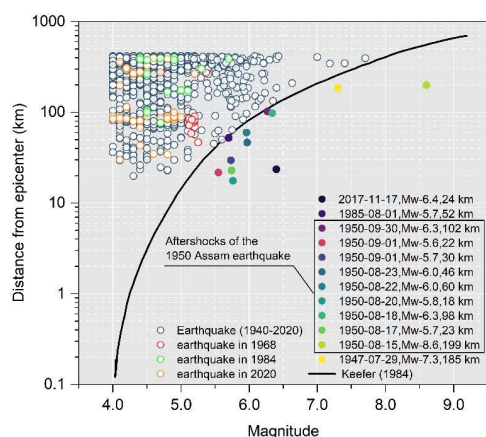


Figure 13: Distance from epicenters of the collected seismic events (1940-2020) to the Zelunglung vs. the seismic magnitude (the black solid curve refers to Keefer (1984)).

Furthermore, we extracted the gridded mean values of annual mean air temperature, summer air temperature, annual precipitation, and summer precipitation within the ZLL catchment during 1940–2021 from a dataset for China (1901–2021) (Peng, 2019) and 1-km monthly precipitation dataset for China (1901–2021) (Peng, 2020), respectively (Fig. 12b and c). These data were validated using 496 independent meteorological observation points (Peng et al., 2019). From 1940 to 2017, the annual mean and summer air temperatures at the ZLL kept relatively stable. However, in 2018, there was a sudden and significant increase in the annual mean and summer air temperatures, with an amplitude exceeding 2.5 °C. Since then, the temperatures have maintained at a high level (Fig. 12c). There has been no significant change in annual and summer precipitation since 1940, but a slight decreasing trend has been observed since 2000 (Fig. 12b). The rates of atmospheric warming in the Tibetan and Himalayan regions are far higher than the general global warming rate since 1960, which accelerates the rates of most glaciers shrinking and ice mass loss across the regions (Shugar et al., 2021; Zhang et al., 2020). Recent studies have shown that the on-going climate warming increases the frequency of such glacier-related slope failures. For instance, the number of rockfalls per decade show a similar growing trend with mean annual air temperature in Chamonix, Mont Blanc massif, France since 1934 (Deline et al., 2015). The frequency of non-seismic rock avalanches in the glaciated Saint Elias Mountains of Alaska was associated with above-average temperatures and is expected to continue increasing with ongoing climate warming (Bessette-Kirton and Coe, 2020). Shugar et al. (2021) suggested that the 2021 Chamoli catastrophic ice-rock avalanche and subsequent mass flow resulted from a complex response of the geologic and topographic settings to regional climate change. Figure 12f highlights four distinct NVA peaks, which likely correspond to small mountain torrents or debris-flows, as suggested by Zhang and Shen (2011). These NVA peaks exhibit a lag of 2–4 years relative to annual mean

批注 [hL27]: Moved to 3.1.2

设置了格式: 字体: 加粗

设置了格式: 字体: 加粗

设置了格式: 字体: 加粗

设置了格式: 字体: 加粗

514 or summer air temperature peaks (Figure-Figs. 12e and 12f). Similarly, the sharp increase in NVA caused by the 2020 debris
515 flow event occurred two years after the 2018 warming anomaly (Figs. 12b and 12d). This lag phenomenon has also been
516 observed in other comparable regions (Deng et al., 2017; Stoffel et al., 2024). Even though there is no direct observation data
517 of surface temperature in the ZLL highland, years of intense warming may change the thermal and hydrological conditions of
518 the ZLL glaciers, such as the thermal regime at the rock-ice contact surface, melting rate of the surface ice and snow, englacial
519 drainage system, fostering the instability of ice-rock blocks on the top. Previous intense seismic shaking could widen rock
520 fractures and reduce the ice-rock strength. It is no doubt that the 2020 ZLL event is the product of the interplay among
521 geological movement, steep topography, and climate warming. However, based on the fact that the lag relationship between
522 the fluctuation peaks of NVAs and temperature fluctuations from 1990 to 2020, it is likely that the 2020 event was triggered
523 by the recent local warming.

524 It is evident that either earthquakes or climate change may increase the occurrence of periglacial debris flows and their sediment
525 yield in southeastern Tibet (Du and Zhang, 1981; Deng et al., 2017; Wang et al., 2023). In the case of ZLL, the NVA closely
526 related to the debris flows decreased until 1990 and slightly fluctuated increased around a low level until 2020. That means
527 the effects of the 1950 earthquake were decaying. The response of hillslopes or glaciers to earthquakes is immediate. Had the
528 2017 Milin earthquake strongly impacted the glaciers in the ZLL, ice-rock failures would have happened a few months later,
529 like in the Sedongpu catchment (Zhang et al., 2022b). By contrast, the response of glaciers to warming will take longer.
530 Meanwhile, approximately one month prior to the 2020 debris flow event, the maximum temperature recorded was 27°C, with
531 a peak precipitation of only 17.5mm. Notably, on the day the 2020 debris flow occurred, the steel bridge deck remained dry,
532 indicating that the precipitation was very light (Peng et al., 2022). On the other hand, the magnitude of the warming-driven
533 debris flows is smaller than that of the earthquake-driven. We believe the abrupt 2.5 °C warming in 2018-2020 is dominant in
534 initiating the 2020 ice-rock avalanche.

535 65.2 Debris flow recurrence intervals and The future risk

536 In catchments where rainfall is the primary triggering process, such as the Multetta catchment in the Alps, debris-flow
537 recurrence intervals have been shown to be insensitive to climate warming (Qie et al., 2024). This is because sediment supply
538 in such catchments is controlled by weathering processes, whose rates are far lower than sediment supply from glaciers,
539 permafrost, or other cryospheric processes. Zhang et al. (2022a) predicted that cryosphere degradation driving the increasing
540 sediment yield in cold regions is likely to shift from a temperature-dependent regime toward a rainfall-dependent one in the
541 next century. But in tectonically active high-altitude areas, the temperature-dependent and the earthquake-dependent regimes
542 will alternate over the coming decades in the future. The case of ZLL demonstrates that glacial detachment caused by the 1950
543 earthquake was not entirely flushed out of the channel but partly remained, providing a large amount of readily available
544 sediment for debris-flow activity over the following forty years, thereby lowering the climate-triggering threshold for debris
545 flows. Trends in NVA suggest that, as the legacy sediment is gradually depleted, debris-flow magnitude and frequency stabilize

设置了格式: 字体颜色: 红色

设置了格式: 字体: (中文)+中文正文 (宋体)

(Fig. 12d), making current debris-flow activity more dependent on climate warming. A similar phenomenon occurred in the nearby periglacial Peilong catchment (Wang et al., 2021b). After decades of quiescence, sediment retained upstream following the 1981–1982 earthquakes created favorable conditions for three large debris flows between 1983 and 1985, after which activity declined. In recent decades, climate warming has promoted sediment accumulation through glacier movement and permafrost thaw, leading to highly active debris flows in 2015. Regardless of the regimes, sediment transport follows a mobilization–storage–remobilization pattern (Berger et al., 2010), and debris-flow recurrence intervals are controlled by the ease of these processes. Under an earthquake-dependent regime, the mobilization and storage phases are brief, with seismic events causing abrupt, large-scale sediment mobilization and substantial immediately available sediment storage; the remobilization of such sediment often requires only a minor triggering threshold. In contrast, under a temperature-dependent regime, sediment mobilization induced by climate-warming-driven glacier and permafrost degradation requires a relatively longer preconditioning period than in earthquake-dependent regime, and debris flows must exceed a higher triggering threshold to remobilize the sediment before it reaches a certain storage magnitude (Savi et al., 2021). Nonetheless, compared with non-glacierized catchments, ZLL still exhibits high sediment mobilization and storage capacity, and once sufficient sediment has accumulated, future hydrological changes induced by climate warming will further facilitate sediment transport (Hirschberg et al., 2020).

The period of the ZLL glacier surges is getting shorter. Zhang (1985) supposed that the surging cycle of the ZLL glacier was about 20 years. According to the latest research by Guillet et al. (2022), the ZLL glacier showed signs of surge in 2004, 2005, and 2006. Moreover, there are more obvious signs of a surge in 2015 (Fig. 14). The interval between the last two surges is ten years, which shows that the surging cycle of the ZLL glacier may be decreasing, and the next large-scale surge may happen in the next ten years. Furthermore, changes in the speed of glacier movement can strongly impact channel side moraines or terminal moraines and lead to slope failures (Richardson and Reynolds, 2000). The potential ice collapse area in the formation area of the ZLL catchment is 2.4 km², the rock collapse area reaches 0.96 km², and the loose moraine accumulation reaches 5.2 km² (Li et al., 2021; Liu et al., 2022). However, the 2020 debris flow was caused by a relatively small area of ice-rock collapses in the formation area, which is only the tip of the iceberg compared to the overall high-risk provenances in the formation area of the ZLL catchment. That means if intense earthquakes or extreme warming events happen not far away from the catchment, the risk of slope failures or glacier detachment on the steep slopes and ridges is high and huge amounts of sediment will be transported into the river by large-scale debris flows.

设置了格式: 字体: 加粗

设置了格式: 字体: (默认) Arial

批注 [hL28]: Reviewer 1
4. Comparison with Other Regions / Studies:
A broader contextualization of the Zelunglung cases in comparable scenarios would be beneficial, particularly with regard to recurrence intervals, mobilized volumes, and downstream effects on river systems. This should be incorporated into the discussion.

Author's response:
Thank you for your suggestion; we have added the relevant discussion.

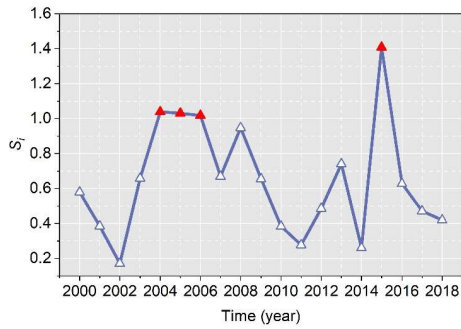


Figure 14: Surge-index (S_i) of Zelunglung Glacier from 2000 to 2018. S_i is a quantitative index of the surge magnitude, calculated by the formula $s_i = \frac{IPR_i}{k \cdot V_0}$, where IPR_i is the inter-percentile range for year i , k is a threshold for surge identification, and V_0 is the error-weighted mean velocity for the study year. The years with $S_i > 1$ are marked with red triangles. (Data source: <https://doi.org/10.5281/zenodo.5524861> (Guillet et al., 2022)).

6.5.3 Effects on river geomorphology

The moraine and old deposits on both ~~channel-sides of the ZLL channel~~ provided numerous boulders for debris flows. The number of coarse particles transported by the ZLL periglacial debris flows is very high, and there is no obvious particle sorting along the flow path. Most of the boulders are gneiss with high hardness, and the wearing and disintegration effects are not significant during the movement along the channel. Coarse particles are deposited on the platform at the bend and the top of the alluvial fan, where the channel suddenly widens. Such phenomenon demonstrates that the movement, deposition, and particle size distribution of the debris flow are not only related to the type of debris flow (Bardou et al., 2003) but also to topographic conditions (Ghilardi et al., 2001; Zhou et al., 2019).

~~In contrast, The the~~ deposition of the 2020 debris flow narrowed the Yarlung Tsangpo River at the outlet of the ZLL, and the river bed was significantly elevated. The river flow hardly transports the boulders on the alluvial fan. The peak discharge of the largest flood in the Yarlung Tsangpo recorded by the hydrologic station at Nuxia, 40 km upstream of the ZLL, is 16800 m³/s. The maximum size of the particles in such a flood is about 150 cm. The floods capable of moving the coarsest boulders (> 600 cm) deposited on the ZLL fan should be on the order of 10⁶ m³/s of peak discharge (Lang et al., 2013). Such high-magnitude floods in the Yarlung Tsangpo were caused by catastrophic breaching of landslide or glacial dams, e.g., several Quaternary megafloods in the middle and downstream of Yarlung Tsangpo (Hu et al., 2018; Liu et al., 2015; Yang et al., 2022), rather than caused by monsoonal runoffs. Modern outburst floods higher than 10⁵ m³/s only happened on the Yigong River, a downstream tributary of the Yarlung Tsangpo Gorge (Hu et al., 2021). Therefore, the time to evacuate the coarse sediments on the alluvial fan is two orders of magnitude of the recurrence period of periglacial debris flows. The long-lived protruding fan forms a knickpoint at the confluence. The repeated glacial and landslide dams in the margin of the Tibetan Plateau play

597 significant roles in reducing the river incision into the plateau interior together with the moraine dams in the glaciation ages
598 (Hu et al., 2021).

599 Comparable processes have been documented in other periglacial catchments. In the Sedongpu catchment, located downstream
600 of ZLL, a sequence of ice-avalanche–debris-flow damming events between 2018 and 2024 repeatedly blocked the Yarlung
601 Tsangpo, triggering frequent channel shifting, narrowing, and bed aggradation(Gao et al., 2023). In Peilong catchment,
602 sustained supply of glacial debris flows has aggraded the channel by ~53 m since 1983. Despite occasional incision by outburst
603 floods, the transport capacity of the main river was insufficient to counteract the persistent input from debris flows, resulting
604 in long-term channel aggradation(Wang et al., 2021b). In Switzerland, the 2025 Birch Glacier collapse mobilized $6 \times 10^6 \text{ m}^3$
605 ice–rock mixture, entraining large quantities of debris and causing significant riverbed aggradation, instantaneously damming
606 the Lonza River and forming a lake that posed considerable geomorphic and hydrological impacts on the downstream valley
607 (Yin et al., 2025). In the Indian Himalaya, the Meru Bamak debris flow transported $\sim 7.9 \times 10^6 \text{ m}^3$ of sediment, with $\sim 6.5 \times$
608 10^6 m^3 deposited at the glacier front. The resulting fan forced the Bhagirathi River to shift ~150 m laterally, fundamentally
609 altering local fluvial morphology(Kumar et al., 2019). These events illustrate that debris flows in periglacial catchments, due
610 to their massive sediment supply and extremely high energy, exert geomorphic impacts far exceeding those of rainfall-triggered
611 events. These processes not only reshape alluvial fans and trunk channels at a local scale, but also profoundly influence river
612 systems through damming, outburst flooding, and channel avulsion. Their impacts are characterized by both sudden
613 catastrophic disturbances and long-term cumulative effects, underscoring the decisive role of periglacial debris flows in
614 shaping river morphology and regulating hydrological processes in high mountain periglacial environments.

615 5.4 Limitation

616 Previous studies have shown that debris-flow volume is often empirically related to the extent of the inundation area (e.g.,
617 Iverson et al., 1998), which supports the use of NVA as a proxy for sediment volume. Multi-periodic periglacial debris flows
618 are strongly associated with variations in the NVA of the alluvial fan, suggesting that NVA can capture long-term trends in
619 debris-flow activity. In practice, however, the NVA includes a fixed portion of the area inundated by the main river and is
620 therefore slightly larger than the actual depositional area caused by debris flows. Technically, the contribution of the main
621 river to NVA cannot be entirely excluded. Nevertheless, the riverbank line remained stable from the 1980s to the 2010s, during
622 which no large periglacial debris flows occurred (Figs. 11b and c; Zhang and Shen, 2011). It is therefore reasonable to assume
623 that variations in river water level have little influence on changes in NVA, and that NVA primarily reflects the relative volume
624 trends of sediment transported by debris flows.

625 Despite these considerations, several uncertainties remain in using NVA as a volume proxy. The absence of systematic
626 depositional thickness measurements prevents direct conversion of NVAs into absolute debris-flow volumes, so NVA only
627 reflects relative fluctuations rather than precise values. Delineation errors in historical imagery, particularly in earlier black-
628 and-white aerial photographs with limited tonal contrast, may affect accuracy. The spatial resolution of imagery also varies

设置了格式: 上标

设置了格式: 上标

批注 [hL29]: Reviewer 1
4. Comparison with Other Regions / Studies:
A broader contextualization of the Zelunglung cases in comparable scenarios would be beneficial, particularly with regard to recurrence intervals, mobilized volumes, and downstream effects on river systems. This should be incorporated into the discussion.

Author's response:
Thank you for your suggestion; we have added the relevant discussion.

设置了格式: 字体: (中文) Times New Roman, 英语(英国)

设置了格式: 突出显示

设置了格式: 突出显示

设置了格式: 突出显示

设置了格式: 字体: 加粗

设置了格式: 突出显示

markedly across decades, which inevitably affects the precision of NVA delineation and may lead to scale-dependent biases when comparing different periods. Error ranges for NVA were plotted to illustrate these uncertainties (Fig. 12d), and although they cannot be entirely eliminated, they do not alter the main analytical results. Moreover, the empirical relationship between inundation area and debris-flow volume may vary with local geomorphic and hydrological conditions, such as fan slope and gully confinement, further complicating volume inference and limiting the applicability of uniform statistical error models. While accurate estimation of sediment volume from NVA is beyond the scope of this study, we acknowledge the associated uncertainties, which warrant more rigorous treatment in future study. Future studies that integrate high-resolution LiDAR, UAV photogrammetry, or borehole surveys with field-based volume measurements could provide more robust statistical assessments of the NVA–volume relationship. The application of dense stereo-pair techniques for DSM extraction from historical and modern satellite archives also has considerable potential to provide three-dimensional constraints on sediment thickness and deposition, thereby improving the translation from inundation area to sediment volume.

7.6 Conclusions

High-magnitude sediment evacuation by periglacial debris flows is a crucial surface process that links sediment yield from high-altitude slopes to river sediment transportation. The ongoing glacier degradation in the Himalayan mountains in response to recent earthquakes and climate change increases the frequency of the debris flows and their sediment volume. The ZLL catchment in the tectonically active eastern Himalayan syntaxis with a high uplift rate has recorded five periglacial debris flow events since 1950. These events delivered huge volumes of sediment into the Yarlung Tsangpo River. We examine the history of the five events and their sediment characteristics, especially the ice-rock-avalanche-triggered event in 2020, through field investigations and remote sensing interpretations. Some findings are concluded as follows:

- a) The periglacial debris flows have great capacities to erode channels, transport sediment, and impact obstacles. The maximum values of the erosion depth, the erosion width, and the impact force near the ZLL outlet are about 20 m, 14 m, and 3.64×10^6 kN, respectively, in the 2020 event. The debris flows transported a high concentration of coarse grains with the size > 50 cm. The 100–300 cm grains account for 77.4% of the coarse grains.
- b) Most of the angular rocks moved by the 2020 avalanche were not delivered downward further. The boulders transported by subsequent debris flows probably originated from the middle of the downstream reaches. The grain size segregation was not observed between the middle reach and the alluvial channel.
- c) The NVA of the ZLL fan reduced from 0.78 km² in 1950 to 0.067 km² in 1990, and kept at a stable low value until 2020, indicating the influence of the 1950 earthquake on the debris-flow sediment transportation could last 40 years. Compared with the 1999 Chi-chi earthquake and the 2008 Wenchuan earthquake in non-glaciated areas, the influence period of the 1950 earthquake is much longer.
- d) The seismic and local meteorological data show that the recent warming events drove the 2020 debris-flow event during 2018–2020. The surging cycle of ZLL glaciers is getting short due to climate change. The correspondence between the

设置了格式: 字体: 加粗

批注 [hl30]: Reviewer 1

1. Quantification of Uncertainties:

- a) The uncertainties in deriving the NVA as a proxy for sediment volume could be treated more rigorously using statistical methods. A quantitative error assessment is missing.
- b) The translation of NVA into actual sediment volumes should be discussed more critically.

Author's changes in manuscript:

We have added a new discussion section (6.4 Limitation) to discuss both the validity and the limitations of using NVA as a proxy

设置了格式: 字体: (中文)+中文正文(宋体), 英语(英国)

recent increases in the local air temperature and the NVA implies that the debris flow occurrences in ZLL transfer from the tectonic-driven to the climatic-driven, with debris flows exhibiting a lagged response of 2–4 years to rising temperatures.

Acknowledgments. This research was funded by the Second Tibetan Plateau Scientific Expedition and Research Program (2019QZKK0902) and the National Natural Science Foundation of China (91747207, 41790434). MRG acknowledges the ‘ANSO Scholarship for Young Talents’ for his postgraduate study.

Data availability. All raw data can be provided by the corresponding authors upon request.

Author contributions. KHH conceptualized the study, interpreted the images, wrote and edited the manuscript. HL analyzed the data and wrote the manuscript draft. KHH, HL, SL, LW, XPZ, and BZ performed the field surveys. HL and MRG collected satellite and background data. LMZ provided constructive suggestions. All authors contributed to the preparation and editing of the paper.

Competing interests. The authors declare that they have no conflict of interests.

References

- Bajracharya, S. R. and Mool, P.: Glaciers, glacial lakes and glacial lake outburst floods in the Mount Everest region, Nepal, ANN GLACIOL, 50, 81–86, <https://doi.org/10.3189/172756410790595895>, 2009.
- Bardou, E., Anczyk, C., Bonnard, C., and Vulliet, L.: Classification of debris-flow deposits for hazard assessment in alpine areas, in: Debris-Flow Hazards Mitigation: Mechanics, Prediction, and Assessment, The Third International Conference on Debris-Flow Hazards Mitigation : Mechanics, Prediction, and Assessment, Davos, Switzerland, 10–12 September 2003, 799–808, ISBN 90-77017-78-X, 2003.
- Berger, C., McArdeell, B. W., and Schlunegger, F.: Sediment transfer patterns at the Illgraben catchment, Switzerland: Implications for the time scales of debris flow activities, GEOMORPHOLOGY, 125, 421–432, <https://doi.org/10.1016/j.geomorph.2010.10.019>, 2010.
- Bessette-Kirton, E. K. and Coe, J. A.: A 36-Year Record of Rock Avalanches in the Saint Elias Mountains of Alaska, With Implications for Future Hazards, FRONT EARTH SC-SWITZ, 8, <https://doi.org/10.3389/feart.2020.00293>, 2020.
- Castino, F., Bookhagen, B., and Strecker, M. R.: Rainfall variability and trends of the past six decades (1950–2014) in the subtropical NW Argentine Andes, CLIM DYNAM, 48, 1049–1067, <https://doi.org/10.1007/s00382-016-3127-2>, 2016.

Chen, D., Xu, B., Yao, T., Guo, Z., Cui, P., Chen, F., Zhang, R., Zhang, X., Zhang, Y., Fan, J., Hou, Z., and Zhang, T.: Assessment of past, present and future environmental changes on the Tibetan Plateau, *Chinese Science Bulletin*, 60, 3025–3035, <https://doi.org/10.1360/n972014-01370>, 2015.

Chen N., Yang C., Li Z., and He J.: Research on the Relationship between the Calculation of Debris flow Velocity and Its Super Elevation in Bend, *Advanced Engineering Sciences*, 41, 165–171, [https://doi.org/1009-3087\(2009\)03-0165-07](https://doi.org/1009-3087(2009)03-0165-07), 2009.

Costa, J. E.: Paleohydraulic reconstruction of flash-flood peaks from boulder deposits in the Colorado Front Range, *GEOL SOC AM BULL.*, 94, 986, [https://doi.org/10.1130/0016-7606\(1983\)94<986:PROFPF>2.0.CO;2](https://doi.org/10.1130/0016-7606(1983)94<986:PROFPF>2.0.CO;2), 1983.

Coudurier-Curveur, A., Tapponnier, P., Okal, E., Van der Woerd, J., Kali, E., Choudhury, S., Baruah, S., Etchebes, M., and Karakaş, Ç.: A composite rupture model for the great 1950 Assam earthquake across the cusp of the East Himalayan Syntaxis, *Earth and Planetary Science Letters*, 531, 115928, <https://doi.org/10.1016/j.epsl.2019.115928>, 2020.

Cui, P., Zhou, G. G. D., Zhu, X. H., and Zhang, J. Q.: Scale amplification of natural debris flows caused by cascading landslide dam failures, *GEOMORPHOLOGY*, 182, 173–189, <https://doi.org/10.1016/j.geomorph.2012.11.009>, 2013.

Cui, Y., Hu, J., Xu, C., Miao, H., and Zheng, J.: Landslides triggered by the 1970 Ms 7.7 Tonghai earthquake in Yunnan, China: an inventory, distribution characteristics, and tectonic significance, *J MT SCI-ENGL*, 19, 1633–1649, <https://doi.org/10.1007/s11629-022-7321-x>, 2022.

Dadson, S. J., Hovius, N., Chen, H., Dade, W. B., Lin, J.-C., Hsu, M.-L., Lin, C.-W., Horng, M.-J., Chen, T.-C., Milliman, J., and Stark, C. P.: Earthquake-triggered increase in sediment delivery from an active mountain belt, *GEOLOGY*, 32, 733, <https://doi.org/10.1130/G20639.1>, 2004.

Dai, L., Scaringi, G., Fan, X., Yunus, A. P., Liu-Zeng, J., Xu, Q., and Huang, R.: Coseismic Debris Remains in the Orogen Despite a Decade of Enhanced Landsliding, *GEOPHYS RES LETT*, 48, <https://doi.org/10.1029/2021GL095850>, 2021.

Deline, P., Gruber, S., Delaloye, R., Fischer, L., Geertsema, M., Giardino, M., Hasler, A., Kirkbride, M., Krautblatter, M., Magnin, F., McColl, S., Ravel, L., and Schoeneich, P.: Ice Loss and Slope Stability in High-Mountain Regions, in: *Snow and Ice-Related Hazards, Risks, and Disasters*, edited by: Shroder, J. F., Haeberli, W., and Whiteman, C., Academic Press, Boston, USA, 521–561, <https://doi.org/10.1016/B978-0-12-394849-6.01001-5>, 2015.

Deng, M., Chen, N., and Liu, M.: Meteorological factors driving glacial till variation and the associated periglacial debris flows in Tianmo Valley, south-eastern Tibetan Plateau, *Nat. Hazards Earth Syst. Sci.*, 17, 345–356, <https://doi.org/10.5194/nhess-17-345-2017>, 2017.

Ding, L., Zhong, D., Yin, A., Kapp, P., and Harrison, T. M.: Cenozoic structural and metamorphic evolution of the eastern Himalayan syntaxis (Namche Barwa), *EARTH PLANET SC LETT*, 192, 423–438, [https://doi.org/10.1016/S0012-821X\(01\)00463-0](https://doi.org/10.1016/S0012-821X(01)00463-0), 2001.

Du R. and Zhang S.: CHARACTERISTICS OF GLACIAL MUD-FLOWS IN SOUTH-EASTERN QINGHAI-XIZANG PLATEAU, *Journal of Glaciology and Geocryology*, 10–16, 81–82, 1981.

Evans, S. G. and Clague, J. J.: Recent climatic change and catastrophic geomorphic processes in mountain environments, in: *Geomorphology and Natural Hazards*, edited by: Morisawa, M., Elsevier, Amsterdam, The Netherlands, 107–128, <https://doi.org/10.1016/B978-0-444-82012-9.50012-8>, 1994.

Frich, P., Alexander, L., Della-Marta, P., Gleason, B., Haylock, M., Klein Tank, A., and Peterson, T.: Observed coherent changes in climatic extremes during the second half of the twentieth century, *CLIM RES*, 19, 193–212, <https://doi.org/10.3354/cr019193>, 2007.

Gao, H., Yin, Y., Li, B., Gao, Y., Zhang, T., Liu, X., and Wan, J.: Geomorphic evolution of the Sedongpu Basin after catastrophic ice and rock avalanches triggered by the 2017 Ms6.9 Milin earthquake in the Yarlung Zangbo River area, China, *LANDSLIDES*, 20, 2327–2341, <https://doi.org/10.1007/s10346-023-02118-3>, 2023.

Ghilardi, P., Natale, L., and Savi, F.: Modeling debris flow propagation and deposition, *Physics and Chemistry of the Earth, Part C: Solar, Terrestrial & Planetary Science*, 26, 651–656, [https://doi.org/10.1016/S1464-1917\(01\)00063-0](https://doi.org/10.1016/S1464-1917(01)00063-0), 2001.

Giorgi, F., Torma, C., Coppola, E., Ban, N., Schär, C., and Somot, S.: Enhanced summer convective rainfall at Alpine high elevations in response to climate warming, *NAT GEOSCI*, 9, 584–589, <https://doi.org/10.1038/ngeo2761>, 2016.

Guillet, G., King, O., Lv, M., Ghuffar, S., Benn, D., Quincey, D., and Bolch, T.: A regionally resolved inventory of High Mountain Asia surge-type glaciers, derived from a multi-factor remote sensing approach, *The Cryosphere*, 16, 603–623, <https://doi.org/10.5194/tc-16-603-2022>, 2022.

Haeberli, W. and Whiteman, C. A. (Eds.): *Snow and ice-related hazards, risks, and disasters*, Elsevier, Amsterdam, The Netherlands, 755pp., <https://doi.org/10.1016/C2018-0-00970-6>, 2021.

Han L. and Feng Q.: Analysis of Development Characteristics and Genetic Mechanisms of Glacier Debris Flows in the Zelongnong, MT. Namjagbarwa, Inner Mongolia Science Technology & Economy, 58–59, <https://doi.org/CNKI:SUN:NMKJ.0.2018-04-029>, 2018.

Hirschberg, J., Fatichi, S., Bennett, G. L., McArde, B. W., Peleg, N., Lane, S. N., Schlunegger, F., and Molnar, P.: Climate Change Impacts on Sediment Yield and Debris-Flow Activity in an Alpine Catchment, *J GEOPHYS RES-EARTH*, 126, e2020JF005739, <https://doi.org/10.1029/2020JF005739>, 2020.

Hu, G., Yi, C.-L., Liu, J.-H., Wang, P., Zhang, J.-F., Li, S.-H., Li, D., Huang, J., Wang, H., Zhang, A., Shi, L., and Shui, X.: Glacial advances and stability of the moraine dam on Mount Namcha Barwa since the Last Glacial Maximum, eastern Himalayan syntaxis, *Geomorphology*, 365, 107246, <https://doi.org/10.1016/j.geomorph.2020.107246>, 2020.

Hu, H.-P., Feng, J.-L., and Chen, F.: Sedimentary records of a palaeo-lake in the middle Yarlung Tsangpo: Implications for terrace genesis and outburst flooding, *QUATERNARY SCI REV*, 192, 135–148, <https://doi.org/10.1016/j.quascirev.2018.05.037>, 2018.

Hu, K., Zhang, X., You, Y., Hu, X., Liu, W., and Li, Y.: Landslides and dammed lakes triggered by the 2017 Ms6.9 Milin earthquake in the Tsangpo gorge, *Landslides*, 16, 993–1001, <https://doi.org/10.1007/s10346-019-01168-w>, 2019.

756 Hu, K., Wu, C., Wei, L., Zhang, X., Zhang, Q., Liu, W., and Yanites, B. J.: Geomorphic effects of recurrent outburst
 757 superfloods in the Yigong River on the southeastern margin of Tibet, SCI REP-UK, 11, 15577, [https://doi.org/10.1038/s41598-](https://doi.org/10.1038/s41598-021-95194-1)
 758 021-95194-1, 2021.
 759 Huang, S., Chen, Y., Burr, G. S., Jaiswal, M. K., Lin, Y. N., Yin, G., Liu, J., Zhao, S., and Cao, Z.: Late Pleistocene sedimentary
 760 history of multiple glacially dammed lake episodes along the Yarlung-Tsangpo river, southeast Tibet, QUATERNARY RES,
 761 82, 430–440, <https://doi.org/10.1016/j.yqres.2014.06.001>, 2014.
 762 Huggel, C., Haeberli, W., Kääb, A., Bieri, D., and Richardson, S.: An assessment procedure for glacial hazards in the Swiss
 763 Alps, CAN GEOTECH J, 41, 1068–1083, <https://doi.org/10.1139/t04-053>, 2004.
 764 Iribarren Anaconda, P., Mackintosh, A., and Norton, K. P.: Hazardous processes and events from glacier and permafrost areas:
 765 lessons from the Chilean and Argentinean Andes, EARTH SURF PROC LAND, 40, 2–21, <https://doi.org/10.1002/esp.3524>,
 766 2015.
 767 Iverson, R. M., Schilling, S. P., and Vallance, J. W.: Objective delineation of lahar-inundation hazard zones, GEOL SOC AM
 768 BULL, 110, 972–984, [https://doi.org/10.1130/0016-7606\(1998\)110<0972:ODOLIH>2.3.CO;2](https://doi.org/10.1130/0016-7606(1998)110<0972:ODOLIH>2.3.CO;2), 1998.
 769 Jia, H., Chen, F., and Pan, D.: Disaster Chain Analysis of Avalanche and Landslide and the River Blocking Dam of the Yarlung
 770 Zangbo River in Milin County of Tibet on 17 and 29 October 2018, IJERPH, 16, 4707, <https://doi.org/10.3390/ijerph16234707>,
 771 2019.
 772 Kääb, A. and Girod, L.: Brief communication: Rapid $\sim 335 \times 10^6 \text{ m}^3$ bed erosion after detachment of the Sedongpu Glacier
 773 (Tibet), CRYOSPHERE, 17, 2533–2541, <https://doi.org/10.5194/tc-17-2533-2023>, 2023.
 774 Kääb, A., Jacquemart, M., Gilbert, A., Leinss, S., Girod, L., Huggel, C., Falaschi, D., Ugalde, F., Petrakov, D., Chernomorets,
 775 S., Dokukin, M., Paul, F., Gascoin, S., Berthier, E., and Kargel, J. S.: Sudden large-volume detachments of low-angle mountain
 776 glaciers – more frequent than thought?, The Cryosphere, 15, 1751–1785, <https://doi.org/10.5194/tc-15-1751-2021>, 2021.
 777 Kargel, J. S., Leonard, G. J., Shugar, D. H., Haritashya, U. K., Bevington, A., Fielding, E. J., Fujita, K., Geertsema, M., Miles,
 778 E. S., Steiner, J., Anderson, E., Bajracharya, S., Bawden, G. W., Breashears, D. F., Byers, A., Collins, B., Dhital, M. R.,
 779 Donnellan, A., Evans, T. L., Geai, M. L., Glasscoe, M. T., Green, D., Gurung, D. R., Heijnen, R., Hilborn, A., Hudnut, K.,
 780 Huyck, C., Immerzeel, W. W., Liming, J., Jibson, R., Kääb, A., Khanal, N. R., Kirschbaum, D., Kraaijenbrink, P. D. A.,
 781 Lamsal, D., Shiyin, L., Mingyang, L., McKinney, D., Nahirnick, N. K., Zhuotong, N., Ojha, S., Olsenholler, J., Painter, T. H.,
 782 Pleasants, M., Pratima, K. C., Yuan, Q. I., Raup, B. H., Regmi, D., Rounce, D. R., Sakai, A., Donghui, S., Shea, J. M., Shrestha,
 783 A. B., Shukla, A., Stumm, D., van der Kooij, M., Voss, K., Xin, W., Weihs, B., Wolfe, D., Lizong, W., Xiaojun, Y., Yoder,
 784 M. R., and Young, N.: Geomorphic and geologic controls of geohazards induced by Nepal’s 2015 Gorkha earthquake,
 785 SCIENCE, 351, aac8353, <https://doi.org/10.1126/science.aac8353>, 2016.
 786 Keefer, D. K.: Landslides caused by earthquakes, Geol Soc America Bull, 95, 406, [https://doi.org/10.1130/0016-](https://doi.org/10.1130/0016-7606(1984)95<406:LCBE>2.0.CO;2)
 787 7606(1984)95<406:LCBE>2.0.CO;2, 1984.

788 Kilburn, C. R. J. and Voight, B.: Slow rock fracture as eruption precursor at Soufriere Hills Volcano, Montserrat, *GEOPHYS*
789 *RES LETT*, 25, 3665–3668, <https://doi.org/10.1029/98GL01609>, 1998.

790 Kumar, A., Bhambri, R., Tiwari, S. K., Verma, A., Gupta, A. K., and Kawishwar, P.: Evolution of debris flow and moraine
791 failure in the Gangotri Glacier region, Garhwal Himalaya: Hydro-geomorphological aspects, *GEOMORPHOLOGY*, 333,
792 152–166, <https://doi.org/10.1016/j.geomorph.2019.02.015>, 2019.

793 Lang, K. A., Huntington, K. W., and Montgomery, D. R.: Erosion of the Tsangpo Gorge by megafloods, Eastern Himalaya,
794 *GEOLOGY*, 41, 1003–1006, <https://doi.org/10.1130/G34693.1>, 2013.

795 Larsen, I. J., Montgomery, D. R., and Korup, O.: Landslide erosion controlled by hillslope material, *NAT GEOSCI*, 3, 247–
796 251, <https://doi.org/10.1038/ngeo776>, 2010.

797 Li, H., Hu, K., Zhang, X., Liu, S., and Wei, L.: Causes and Damage of the 2020 Periglacial Debris Flows at Zelunglung
798 Catchment in the Eastern Syntaxis of Himalaya, in: *Engineering Geology for a Habitable Earth: IAEG XIV Congress 2023*
799 *Proceedings*, IAEG 2023, Chengdu, China, 21–27 September 2023, 161–171, https://doi.org/10.1007/978-981-99-9061-0_12,
800 2024a.

801 Li, H., Liu, S., Hu, K., and Zhang, X.: Differential depression of the glacier equilibrium-line altitudes in the Yarlung Zangbo
802 Downstream Basin in the Last Glacial Maximum compared to the pre-industrial era, *J GEOGR SCI*, 34, 1157–1173,
803 <https://doi.org/10.1007/s11442-024-2243-x>, 2024b.

804 Li, J., Chu, H., Li, B., Gao, Y., Wang, M., Zhao, C., and Liu, X.: Analysis of development characteristics of high-
805 elevation chain geological hazard in Zelongnong, Nyingchi, Tibet based on high resolution image and InSAR interpretation,
806 *The Chinese Journal of Geological Hazard and Control*, 32, 42–50, [https://doi.org/10.16031/j.cnki.issn.1003-8035.2021.03-](https://doi.org/10.16031/j.cnki.issn.1003-8035.2021.03-06)
807 06, 2021.

808 Li, W., Zhao, B., Xu, Q., Scaringi, G., Lu, H., and Huang, R.: More frequent glacier-rock avalanches in Sedongpu gully are
809 blocking the Yarlung Zangbo River in eastern Tibet, *LANDSLIDES*, 19, 589–601, [https://doi.org/10.1007/s10346-021-01798-](https://doi.org/10.1007/s10346-021-01798-z)
810 z, 2022.

811 Li Y., Yan C., Hu K., and Wei L.: VARIATION OF HAZARD AREAS OF TYPICAL RAINSTORM DEBRIS FLOW
812 ALLUVIAL FANS, *Resources and Environment in the Yangtze Basin*, 26, 789–796,
813 <https://doi.org/10.11870/cjlyzyyhj201705017>, 2017.

814 Liu, M., Zhang, Y., Tian, S., Chen, N., Mahfuz, R., and Javed, I.: Effects of loose deposits on debris flow processes in the
815 Aizi Valley, southwest China, *J MT SCI-ENGL*, 17, 156–172, <https://doi.org/10.1007/s11629-019-5388-9>, 2020.

816 Liu, W., Lai, Z., Hu, K., Ge, Y., Cui, P., Zhang, X., and Liu, F.: Age and extent of a giant glacial-dammed lake at Yarlung
817 Tsangpo gorge in the Tibetan Plateau, *GEOMORPHOLOGY*, 246, 370–376, <https://doi.org/10.1016/j.geomorph.2015.06.034>,
818 2015.

819 Liu, W., Wang, M., Song, B., Yu, T., Huang, X., Jiang, Y., and Sun, Y.: Surveys and chain structure study of potential hazards
820 of ice avalanches based on optical remote sensing technology: A case study of southeast Tibet, *Remote Sensing for Natural*
821 *Resources*, 34, 265–276, <https://doi.org/10.6046/zrzyyg.2021076>, 2022.

822 Liu, Y., Montgomery, D. R., Hallet, B., Tang, W., Zhang, J., and Zhang, X.: QUATERNARY GLACIER BLOCKING
823 EVENTSAT THE ENTRANCE OF YARLUNG ZANGBO GREAT CANYON, SOUTHEAST TIBET, *Quaternary Sciences*,
824 52–62, <https://doi.org/10.3321/j.issn:1001-7410.2006.01.007>, 2006.

825 Luan L. and Zhai P.: hanges in rainy season precipitation properties over the Qinghai-Tibet Plateau based on multi-source
826 datasets, *Climate Change Research*, 173–190, 2023.

827 Major, J. J.: Pebble orientation on large, experimental debris-flow deposits, *SEDIMENT GEOL*, 117, 151–164,
828 [https://doi.org/10.1016/S0037-0738\(98\)00014-1](https://doi.org/10.1016/S0037-0738(98)00014-1), 1998.

829 McCoy, S. W., Tucker, G. E., Kean, J. W., and Coe, J. A.: Field measurement of basal forces generated by erosive debris flows,
830 *J GEOPHYS RES-EARTH*, 118, 589–602, <https://doi.org/10.1002/jgrf.20041>, 2013.

831 Montgomery, D. R., Hallet, B., Yuping, L., Finnegan, N., Anders, A., Gillespie, A., and Greenberg, H. M.: Evidence for
832 Holocene megafloods down the tsangpo River gorge, Southeastern Tibet, *QUATERNARY RES*, 62, 201–207,
833 <https://doi.org/10.1016/j.yqres.2004.06.008>, 2004.

834 Myhre, G., Alterskjær, K., Stjern, C. W., Hodnebrog, Ø., Marelle, L., Samset, B. H., Sillmann, J., Schaller, N., Fischer, E.,
835 Schulz, M., and Stohl, A.: Frequency of extreme precipitation increases extensively with event rareness under global warming,
836 *SCI REP-UK*, 9, 16063, <https://doi.org/10.1038/s41598-019-52277-4>, 2019.

837 Parker, R. N., Densmore, A. L., Rosser, N. J., de Michele, M., Li, Y., Huang, R., Whadcoat, S., and Petley, D. N.: Mass wasting
838 triggered by the 2008 Wenchuan earthquake is greater than orogenic growth, *Nature Geosci*, 4, 449–452,
839 <https://doi.org/10.1038/ngeo1154>, 2011.

840 Peng, D., Zhang, L., Jiang, R., Zhang, S., Shen, P., Lu, W., and He, X.: Initiation mechanisms and dynamics of a debris flow
841 originated from debris-ice mixture slope failure in southeast Tibet, China, *Engineering Geology*, 307, 106783,
842 <https://doi.org/10.1016/j.enggeo.2022.106783>, 2022.

843 Peng, S.: 1-km monthly mean temperature dataset for china (1901-2023), National Tibetan Plateau Data Center [data set],
844 <https://doi.org/10.11888/Meteoro.tpd.270961>, 2019.

845 Peng, S.: 1-km monthly precipitation dataset for China (1901-2023), National Tibetan Plateau / Third Pole Environment Data
846 Center [data set], <https://doi.org/10.5281/zenodo.3114194>, 2020.

847 Peng, S., Ding, Y., Liu, W., and Li, Z.: 1 km monthly temperature and precipitation dataset for China from 1901 to 2017,
848 *EARTH SYST SCI DATA*, 11, 1931–1946, <https://doi.org/10.5194/essd-11-1931-2019>, 2019.

849 Petrakov, D. A., Krylenko, I. V., Chernomorets, S. S., Tutubalina, O. V., Krylenko, I. N., and Shakhmina, M. S.: Debris flow
850 hazard of glacial lakes in the Central Caucasus, in: *Debris-Flow Hazards Mitigation: Mechanics, Prediction, and Assessment*,

851 The Fourth International Conference on Debris-Flow Hazards Mitigation: Mechanics, Prediction, and Assessment, Chengdu,
852 China, 10-13 September 2007, 703–714, ISBN 9789059660595, 2007.

853 Qie, J., Favillier, A., Liébault, F., Ballesteros Cánovas, J. A., Lopez-Saez, J., Guillet, S., Francon, L., Zhong, Y., Stoffel, M.,
854 and Corona, C.: A supply-limited torrent that does not feel the heat of climate change, *NAT COMMUN*, 15, 9078,
855 <https://doi.org/10.1038/s41467-024-53316-z>, 2024.

856 RGI, C.: Randolph Glacier Inventory - A Dataset of Global Glacier Outlines, Version 7,
857 <https://doi.org/10.5067/F6JMOVY5NAVZ>, 2023.

858 Richardson, S. D. and Reynolds, J. M.: An overview of glacial hazards in the Himalayas, *Quaternary International*, 65–66, 31–
859 47, [https://doi.org/10.1016/S1040-6182\(99\)00035-X](https://doi.org/10.1016/S1040-6182(99)00035-X), 2000.

860 Savi, S., Comiti, F., and Strecker, M. R.: Pronounced increase in slope instability linked to global warming: A case study from
861 the eastern European Alps, *EARTH SURF PROC LAND*, 46, 1328–1347, <https://doi.org/10.1002/esp.5100>, 2021.

862 Shen, Y., Su, H., Wang, G., Mao, W., Wang, S., Han, P., Wang, N., and Li, Z.: The Responses of Glaciers and Snow Cover to
863 Climate Change in Xinjiang (II): Hazards Effects, *Journal of Glaciology and Geocryology*, 35, 1355–1370, 2013.

864 Shugar, D. H., Jacquemart, M., Shean, D., Bhushan, S., Upadhyay, K., Sattar, A., Schwanghart, W., McBride, S., de Vries, M.
865 V. W., Mergili, M., Emmer, A., Deschamps-Berger, C., McDonnell, M., Bhambri, R., Allen, S., Berthier, E., Carrivick, J. L.,
866 Clague, J. J., Dokukin, M., Dunning, S. A., Frey, H., Gascoin, S., Haritashya, U. K., Huggel, C., Kääb, A., Kargel, J. S.,
867 Kavanaugh, J. L., Lacroix, P., Petley, D., Rupper, S., Azam, M. F., Cook, S. J., Dimri, A. P., Eriksson, M., Farinotti, D., Fiddes,
868 J., Gnyawali, K. R., Harrison, S., Jha, M., Koppes, M., Kumar, A., Leinss, S., Majeed, U., Mal, S., Muhuri, A., Noetzli, J.,
869 Paul, F., Rashid, I., Sain, K., Steiner, J., Ugalde, F., Watson, C. S., and Westoby, M. J.: A massive rock and ice avalanche
870 caused the 2021 disaster at Chamoli, Indian Himalaya, *Science*, 373, 300–306, <https://doi.org/10.1126/science.abh4455>, 2021.

871 Sohn, Y. K.: Coarse-grained debris-flow deposits in the Miocene fan deltas, SE Korea: a scaling analysis, *SEDIMENT GEOL*,
872 130, 45–64, [https://doi.org/10.1016/S0037-0738\(99\)00099-8](https://doi.org/10.1016/S0037-0738(99)00099-8), 2000.

873 Stoffel, M., Trappmann, D. G., Coullie, M. I., Ballesteros Cánovas, J. A., and Corona, C.: Rockfall from an increasingly
874 unstable mountain slope driven by climate warming, *NAT GEOSCI*, 17, 249–254, [https://doi.org/10.1038/s41561-024-01390-](https://doi.org/10.1038/s41561-024-01390-9)
875 9, 2024.

876 Tian, L., Yao, T., Gao, Y., Thompson, L., Mosley-Thompson, E., Muhammad, S., Zong, J., Wang, C., Jin, S., and Li, Z.: Two
877 glaciers collapse in western Tibet, *J GLACIOL*, 63, 194–197, <https://doi.org/10.1017/jog.2016.122>, 2017.

878 Wang, H., Wang, B.-B., Cui, P., Ma, Y.-M., Wang, Y., Hao, J.-S., Wang, Y., Li, Y.-M., Sun, L.-J., Wang, J., Zhang, G.-T.,
879 Li, W.-M., Lei, Y., Zhao, W.-Q., Tang, J.-B., and Li, C.-Y.: Disaster effects of climate change in High Mountain Asia: State
880 of art and scientific challenges, *ADV CLIM CHANG RES*, 15, 367–389, <https://doi.org/10.1016/j.accre.2024.06.003>, 2024.

881 Wang, J., Jin, Z., Hilton, R. G., Zhang, F., Densmore, A. L., Li, G., and West, A. J.: Controls on fluvial evacuation of sediment
882 from earthquake-triggered landslides, *Geology*, 43, 115–118, <https://doi.org/10.1130/G36157.1>, 2015.

883 Wang, P., Wang, H., Hu, G., Qin, J., and Li, C.: A preliminary study on the development of dammed paleolakes in the Yarlung
884 Tsangpo River basin, southeastern Tibet, *Earth Science Frontiers*, 28, 35–45, <https://doi.org/10.13745/j.esf.sf.2020.9.18>, 2021a.
885 Wang, Z., Hu, K., Ma, C., Li, Y., and Liu, S.: Landscape change in response to multiperiod glacial debris flows in Peilong
886 catchment, southeastern Tibet, *J. Mt. Sci.*, 18, 567–582, <https://doi.org/10.1007/s11629-020-6172-6>, 2021b.
887 Wang, Z., Hu, K., and Liu, S.: Classification and sediment estimation for debris flow-prone catchments in the Parlung Zangbo
888 Basin on the southeastern Tibet, *Geomorphology*, 413, 108348, <https://doi.org/10.1016/j.geomorph.2022.108348>, 2022.
889 Wang, Z., Ma, C., Hu, K., Liu, S., and Lyu, L.: Investigation of initiation conditions of periglacial debris flows in Sanggu
890 watershed, Eastern Himalayas, Tibet Plateau (China), *LANDSLIDES*, 20, 813–827, [https://doi.org/10.1007/s10346-022-](https://doi.org/10.1007/s10346-022-02003-5)
891 [02003-5](https://doi.org/10.1007/s10346-022-02003-5), 2023.
892 Ward, F. K.: Explorations in South-Eastern Tibet, *GEOGR J*, 67, 97, <https://doi.org/10.2307/1783136>, 1926.
893 Wu, X., Xu, X., Yu, G., Ren, J., Yang, X., Chen, G., Xu, C., Du, K., Huang, X., Yang, H., Li, K., and Hao, H.: The China
894 Active Faults Database (CAFD) and its web system, *EARTH SYST SCI DATA*, 16, 3391–3417, [https://doi.org/10.5194/essd-](https://doi.org/10.5194/essd-16-3391-2024)
895 [16-3391-2024](https://doi.org/10.5194/essd-16-3391-2024), 2024.
896 Yan, Y., Tang, H., Hu, K., Turowski, J. M., and Wei, F.: Deriving Debris-Flow Dynamics From Real-Time Impact-Force
897 Measurements, *J GEOPHYS RES-EARTH*, 128, e2022JF006715, <https://doi.org/10.1029/2022JF006715>, 2023.
898 Yang, A., Wang, H., Liu, W., Hu, K., Liu, D., Wu, C., and Hu, X.: Two megafloods in the middle reach of Yarlung Tsangpo
899 River since Last-glacial period: Evidence from giant bars, *GLOBAL PLANET CHANGE*, 208, 103726,
900 <https://doi.org/10.1016/j.gloplacha.2021.103726>, 2022.
901 Yin Y., Zhang S., Huo Z., Yang C., and Chen F.: Study on the May 28 Birch high-altitude and long-runout ice-rock avalanche
902 in the Swiss Alps, *The Chinese Journal of Geological Hazard and Control*, 1–14, [https://doi.org/10.16031/j.cnki.issn.1003-](https://doi.org/10.16031/j.cnki.issn.1003-8035.202507033)
903 [8035.202507033](https://doi.org/10.16031/j.cnki.issn.1003-8035.202507033), 2025.
904 Yu, G., Yao, W., Huang, H. Q., and Liu, Z.: Debris flows originating in the mountain cryosphere under a changing climate: A
905 review, *Progress in Physical Geography: Earth and Environment*, 45, 339–374, <https://doi.org/10.1177/0309133320961705>,
906 2021.
907 Zhang, G., Yao, T., Xie, H., Yang, K., Zhu, L., Shum, C. K., Bolch, T., Yi, S., Allen, S., Jiang, L., Chen, W., and Ke, C.:
908 Response of Tibetan Plateau lakes to climate change: Trends, patterns, and mechanisms, *EARTH-SCI REV*, 208, 103269,
909 <https://doi.org/10.1016/j.earscirev.2020.103269>, 2020.
910 Zhang, J. and Shen, X.: Debris-flow of Zelongnong Ravine in Tibet, *J. Mt. Sci.*, 8, 535–543, [https://doi.org/10.1007/s11629-](https://doi.org/10.1007/s11629-011-2137-0)
911 [011-2137-0](https://doi.org/10.1007/s11629-011-2137-0), 2011.
912 Zhang, T., Li, D., East, A. E., Walling, D. E., Lane, S., Overeem, I., Beylich, A. A., Koppes, M., and Lu, X.: Warming-driven
913 erosion and sediment transport in cold regions, *NAT REV EARTH ENV*, 3, 832–851, [https://doi.org/10.1038/s43017-022-](https://doi.org/10.1038/s43017-022-00362-0)
914 [00362-0](https://doi.org/10.1038/s43017-022-00362-0), 2022a.

915 Zhang, T., Wang, W., Shen, Z., and An, B.: Increasing frequency and destructiveness of glacier-related slope failures under
916 global warming, *SCI BULL*, 69, 30–33, <https://doi.org/10.1016/j.scib.2023.09.042>, 2023.

917 Zhang W.: Some features of the surge glacier in the MT. Namjagbarwa, *Mountain Research*, 234–238, 1985.

918 Zhang, W.: Identification of glaciers with surge characteristics on the Tibetan Plateau, *Ann. Glaciol.*, 16, 168–172,
919 <https://doi.org/10.3189/1992AoG16-1-168-172>, 1992.

920 Zhang, X., Hu, K., Liu, S., Nie, Y., and Han, Y.: Comprehensive interpretation of the Sedongpu glacier-related mass flows in
921 the eastern Himalayan syntaxis, *J. Mt. Sci.*, 19, 2469–2486, <https://doi.org/10.1007/s11629-022-7376-8>, 2022b.

922 Zhou, G. G. D., Li, S., Song, D., Choi, C. E., and Chen, X.: Depositional mechanisms and morphology of debris flow: physical
923 modelling, *LANDSLIDES*, 16, 315–332, <https://doi.org/10.1007/s10346-018-1095-9>, 2019.

924 Zhu, S., Wu, W., Zhao, X., Li, J., and Wang, H.: Middle-Late Pleistocene Glacial Lakes in the Grand Canyon of the Tsangpo
925 River, Tibet, *Acta Geologica Sinica (Eng)*, 86, 266–283, <https://doi.org/10.1111/j.1755-6724.2012.00627.x>, 2012.

926

Reviewer 1

c) **For the differential elevation models shown, stable areas should also be presented, and the DoD values in those areas should be critically discussed. At minimum, the arithmetic mean, RMSE, maximum value, minimum value, and standard deviation should be reported.**

Thank you for your suggestion. We have improved this part in the first revision. The reconstruction and differencing of DSMs are carried out in Pix4DMapper and Arcmap10.8. Since we did not deploy ground control points during drone photography, we generated DSM and DOM of September 9 in Pix4DMapper, and then selected 20 relatively stable points that were not affected by debris flow events as control points in Arcmap with DOM of September 9 as reference. These control points were then used in Pix4DMapper to generate the September 11 DSM and DOM. To determine the uncertainty for our UAV DSMs of difference (DoD) differencing result we follow methods outlined in Shugar et al. (2021). We identified a series of fifteen stable areas on old debris flow terraces adjacent to the valley floor (Mainly roads and unseeded farmlands) and retrieved the standard deviation of DoD values within these areas and used these to estimate a two-sigma DoD uncertainty. The resulting elevation uncertainty was ± 0.493 m, corresponding to a DoD volumetric uncertainty of $\pm 1.85 \times 10^4$ m³ (Line 422). Owing to the large extent of the study area, and to avoid redundancy while presenting geomorphic changes in the debris-flow impact zone more clearly, we did not include the results from the stable areas in the manuscript figure, but we provide them here in this response (Fig. S1).

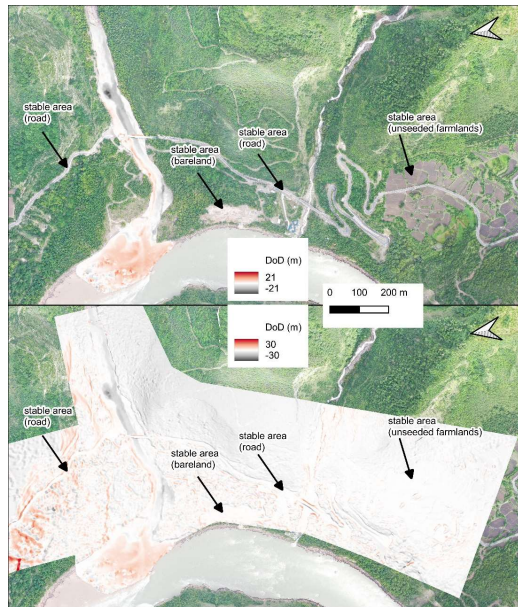


Figure S1. DoD results for the debris-flow inundation zone and geomorphically stable areas.

Reviewer 1

6. Entire Results Chapter:

There is already extensive discussion included in the results chapter. A better separation between the results and the actual discussion would be desirable. This would give the paper a clearer structure and organization. Alternatively, the results and discussion could be merged into a single chapter. However, the current chapter structure suggests a clear separation between results and discussion, whereas in the text, these two sections blur together, and the actual discussion is ultimately rather brief.

Author's response:

Thank you for your suggestion. We have reorganized the structure of the manuscript.

We moved the “4.1 Rapid glacier changes” section to the study area description, as it is based on literature review. The “5 Multi-periodic Sedimentation in the Confluence” section was incorporated into “4 Results.” The final “4 Results” section is divided into three subsections: “4.1 Multi-periodic glacial debris flows,” “4.2 Sediment characteristics of the 2020 event,” and “4.3 Multi-periodic sedimentation

in the confluence.” We consider these three subsections to present direct conclusions derived from our methods, including the basic characteristics of historical debris flows, detailed sedimentary features of the 2020 event, and the interpreted distribution of non-vegetated areas (NVA).

In the Discussion, the original “6.1 The dominant factor and future risk” was split into “5.1 The dominant factor for debris flows and sediment yield” and “5.2 Debris flow recurrence intervals and future risk.” We provide a more in-depth discussion of earthquake and climate influences, linking different events, NVA changes, and the effects of climate and seismic activity. In “5.2 Debris flow recurrence intervals and future risk” and “5.3 Effects on river geomorphology,” we performed comparative analyses addressing reviewer comments on recurrence intervals, sediment mobilization, and downstream impacts on the river system. A new subsection, “5.4 Limitations,” was added to discuss methodological uncertainties and directions for future research.

第 25 页: [3] 批注 [hL19]

ho Lee

2025/9/6 22:14:00

Reviewer 1

k) **Line 331: The value range of the DoD figure should be symmetrically centered around zero (e.g., –21 m to +21 m) to visually balance erosion and deposition and facilitate interpretation. Stable areas should also be shown, and a DoD error assessment should be carried out.**

Author's response:

Thank you for your suggestion. We have updated the DoD range to –21 m to +21 m (Fig. 10). In our first revision, we quantified the DoD uncertainty as $\pm 1.85 \times 10^4 \text{ m}^3$ (Line 422). Owing to the large extent of the study area, and to avoid redundancy while presenting geomorphic changes in the debris-flow impact zone more clearly, we did not include the results from the stable areas in the manuscript figure, but we provide them here in this response (Fig. S1).

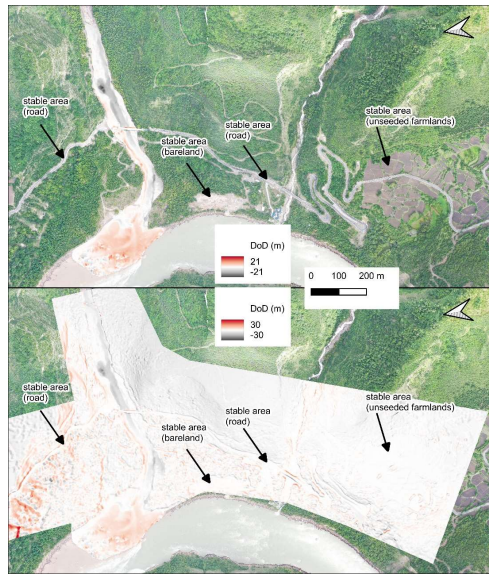


Figure S1. DoD results for the debris-flow inundation zone and geomorphically stable areas.

Reviewer 1

k) **Line 331: The value range of the DoD figure should be symmetrically centered around zero (e.g., -21 m to +21 m) to visually balance erosion and deposition and facilitate interpretation. Stable areas should also be shown, and a DoD error assessment should be carried out.**

Author's response:

Thank you for your suggestion. We have updated the DoD range to -21 m to +21 m (Fig. 10). In our first revision, we quantified the DoD uncertainty as $\pm 1.85 \times 10^4 \text{ m}^3$ (Line 422). Owing to the large extent of the study area, and to avoid redundancy while presenting geomorphic changes in the debris-flow impact zone more clearly, we did not include the results from the stable areas in the manuscript figure, but we provide them here in this response (Fig. S1).

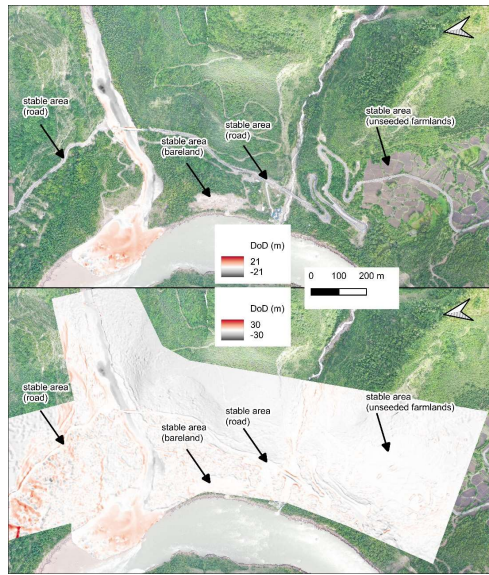


Figure S1. DoD results for the debris-flow inundation zone and geomorphically stable areas.

Reviewer 2

1. **Page 20, line 74. Could part of the material be submerged? more likely it was eroded and washed away by powerful Yarlung Tsangpo stream.**

Author's response:

Thank you for your suggestion. Yes, our consideration here was indeed not comprehensive. In fact, the ZLL debris-flow deposits contain a high proportion of boulders and coarse particles (as noted in the section 4.2.2), so some of the boulders may have been temporarily submerged by the river, but they are unlikely to be transported away by the strong flow of the Yarlung Tsangpo River. Meanwhile, the fine-grained sediments within the debris flow could indeed be eroded and carried away by the main river, resulting in partial sediment loss. We have accordingly revised the relevant statements in the main tex